

# Low-cost Sensors Data Fusion for Small Size Unmanned Aerial Vehicles Navigation and Guidance

Roberto Sabatini<sup>1</sup>✉, Subramanian Ramasamy<sup>2</sup>, Alessandro Gardi<sup>2</sup>  
and Leopoldo Rodriguez Salazar<sup>2</sup>.

1. School of Aerospace, Mechanical and Manufacturing Engineering, RMIT University, Australia.

2. AEROTECH Systems Ltd, United Kingdom.

**Abstract:** Sabatini R, Ramasamy S, Gardi A and Rodriguez-Salazar L. (2013). Low-cost sensors data fusion for small size unmanned aerial vehicles navigation and guidance. *International Journal of Unmanned Systems Engineering*. 1(3): 16-47. A new integrated navigation system designed for small size Unmanned Aerial Vehicles (UAVs) is presented. The proposed system is based on a number of low-cost avionics sensors, including Global Navigation Satellite Systems (GNSS), Micro-Electro-Mechanical System (MEMS) based Inertial Measurement Unit (IMU) and Vision Based Sensors (VBS). The use of an Aircraft Dynamics Models (ADMs) to provide additional information to compensate for the shortcomings of Vision Based Navigation (VBN) and MEMS-IMU sensors in high-dynamics attitude determination tasks is also considered. Additionally, the research concentrates on the potential of carrier-phase GNSS for Attitude Determination (GAD) using interferometric techniques. The main objective is to design a compact, light and relatively inexpensive system capable of providing the required navigation performance (position and attitude data) in all phases of flight of small UAVs, with a special focus on precision approach and landing, where VBN techniques can be fully exploited in a multi-sensor data fusion architecture. An Extended Kalman Filter (EKF) is developed to integrate the information provided by the different sensors and to provide estimates of position, velocity and attitude of the UAV platform in real-time. Three different integrated navigation system architectures are implemented. The first architecture uses VBN at 20 Hz and GNSS at 1 Hz to augment the MEMS-IMU running at 100 Hz. The second mode also includes the ADM (computations performed at 100 Hz) to provide augmentation of the attitude channel. The third fusion architecture uses GNSS based attitude values. The simulations are carried out on the AEROSONDE UAV performing high-dynamics manoeuvres representative of the UAV operational flight envelope. Simulation of the VBN-IMU-GNSS (VIG) integrated navigation system shows that the system can attain position, velocity and attitude accuracies complying with Category Two

## Keywords:

Unmanned aerial vehicle  
Vision based navigation  
MEMS inertial measurement unit  
GNSS  
GNSS attitude determination  
Low-cost navigation sensors and EKF



## Correspondence

RMIT University  
Building 57, Level 3, Office 36  
114 Queensberry Street  
Carlton, VIC 3053, Australia  
[roberto.sabatini@rmit.edu.au](mailto:roberto.sabatini@rmit.edu.au)  
[www.rmit.edu.au](http://www.rmit.edu.au)

(CAT II) precision approach requirements. Simulation of the VBN-IMU-GNSS-ADM (VIGA) system also shows promising results, since the achieved attitude accuracy is higher using the ADM-VBN-IMU than using VBN-IMU only. However, due to rapid divergence of the ADM virtual sensor, there is a need for frequent re-initialisation of the ADM data module, which is strongly dependent on the UAV flight dynamics and the specific manoeuvring transitions performed. In the simulation of the third integrated navigation system, the VIG system is augmented by employing the GAD, forming the VIG-GAD (VIGGA) system architecture. The performances achieved with the VIG, VIGA and VIGGA integrated Navigation and Guidance System (NGS) are presented and are in line with the International Civil Aviation Organization (ICAO) precision approach requirements.

© Marques Aviation Ltd.

## 1. INTRODUCTION

Unmanned Aerial Vehicles (UAVs) are increasingly used in both civil and military applications as they provide cost-effective and safe alternatives to manned aircraft, especially in Dull, Dirty and Dangerous (D3) roles. From an operational perspective, UAVs have the capability of performing tasks with higher degree of manoeuvrability and long endurance. UAV mission- and safety-critical tasks are strongly affected by the integrity management strategies in place to address navigation, communication and surveillance requirements. For effective separation between aircraft and UAVs, the Performance Based Navigation (PBN) approach enforces a set of Required Navigation Performance (RNP) standards related to the different flight phases.<sup>[1]</sup> These required performances are, in turn, translated to technical requirements, which constraint the selection of sensor candidates. Requirements for air navigation systems primarily include accuracy, physical characteristics such as weight and volume, support requirements such as electrical power, and system integrity. One of the most important applications is to use a multi-sensor integrated system to cope with the requirements of long/medium range navigation and landing. This would reduce cost, weight/volume and support requirements and, with the appropriate sensors and integration architecture, give increased accuracy and integrity of the overall system. The best candidates for such integration are indeed satellite navigation and inertial sensors. Computer vision has played an important role in the development of UAVs.<sup>[2]</sup> VBN sensors provide a self-contained autonomous navigation solution and hence they are used as an alternative (or an addition) to more traditional sensors like Global Navigation Satellite Systems (GNSS) and Inertial Navigation System (INS).<sup>[3]</sup> In the current scenario, Micro-Electro-Mechanical System (MEMS) based Inertial Measurement Units (IMU), which are low-cost and low-volume/weight sensors are particularly well suited for small/medium size UAV applications. Regarding the VBN sensors, it was observed that the image processing frontend was susceptible to false detection of the horizon if any other strong edges were present in the image.<sup>[4]</sup> Therefore, an Extended Kalman Filter (EKF) is typically implemented to filter out these incorrect results. The VBN sensor has to be specifically tailored for approach/landing applications (i.e., the most demanding and potentially safety-critical flight phase). The possible synergies attainable from the integration of GNSS Attitude Determination (GAD) systems and Aircraft Dynamics Model (ADM) with VBN and MEMS-INS were also considered.<sup>[5]</sup> In line with the above discussions, the main objective of our research is to develop a low-cost and low-weight/volume Navigation and Guidance System (NGS) based on VBN and other low-cost and low-weight/volume sensors, capable of providing the required level of performance in all flight phases of a small size UAV, with a special focus on precision approach and landing, where VBN techniques can be fully exploited in a multisensory integrated architecture. In addition to developing integrated

navigation sensors, the data provided by the NGC loop were used to optimise the design of a hybrid control system, tailored for VBN, which employs Fuzzy logic and Proportional/Integral/Derivative (PID) techniques. This allows the development of an integrated NGS capable of providing the required level of performance in all flight phases of a small UAV.<sup>[6]</sup> In this paper, a detailed case study is performed in a high dynamics UAV application, employing a Six-Degree-of-Freedom (6DOF) model as the ADM.

## 2. MULTI-SENSOR CHOICES FOR DATA FUSION

A number of sensors can be considered as potential candidates for data fusion. In our research, we developed an integrated NGS approach employing two state-of-the-art physical sensors: MEMS-based INS and GNSS, as well as augmentation from ADM which acts as a virtual sensor and visual sensors in specific flight phases (low altitude). Our previous research activities<sup>[4-6]</sup> presented the various sensors considered for integration. A simplified block diagram of the various candidate sensors is illustrated in Fig. 1.

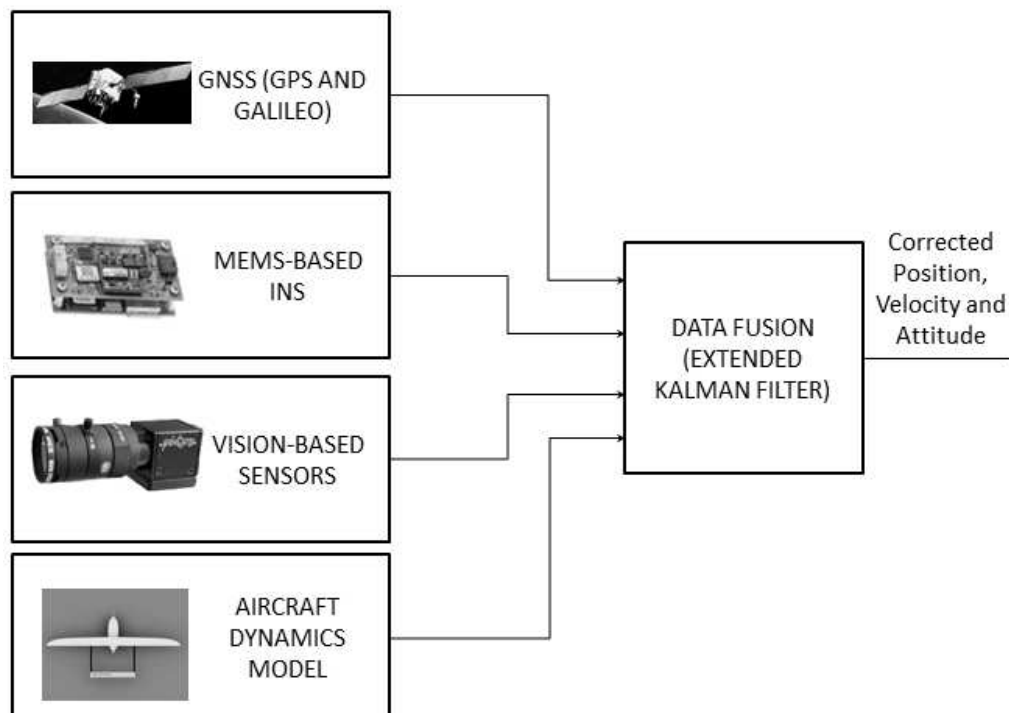


**Fig. 1: Sensors utilised for data fusion**

GNSS and INS are the primary data fusion candidates. GNSS can provide high-accuracy position and velocity data using pseudorange, carrier phase, Doppler observables or various combinations of these measurements. Global Positioning System (GPS) Standard Positioning Service (SPS) pseudorange measurements are considered for position and velocity computations. Typically, GPS position and velocity measurements are provided at a rate of 1 Hz. GNSS Carrier Phase Measurements (CFM) are utilised for attitude estimation. The concept of replacing traditional attitude sensors with GNSS interferometric processing (carrier-phase) has been also considered in recent years, mostly for spacecraft applications (replacing or aiding traditional sun-sensors, horizon-trackers, star-trackers, magnetometers, etc.), and for manned aircraft<sup>[7-9]</sup> and ship applications<sup>[10]</sup>. Due to the low volume/weight of current carrier-phase GNSS receivers, and the extremely high accuracy attainable notwithstanding their lower cost, interferometric GNSS technology is becoming an excellent candidate for future UAV applications.<sup>[11]</sup> Several methods have been developed in the past for GAD systems. The classical method, developed in [12], involves two main steps. The first step is to find a matrix that transforms the baseline configurations to an equivalent orthonormal basis and the second step is the use of fast algorithms (e.g., QUEST and

FOAM) for attitude determination. An alternative method is to adopt recursive algorithms to minimize a cost function that links all available carrier phase measurements.<sup>[5]</sup> Independently from the method selected, since GAD errors are dominated by lengths of the baselines used, some efficient geometric algorithms have been proposed for baseline selection in the presence of redundant satellite measurements. The accuracy of the GAD systems is affected by several factors including the selected equipment/algorithms and the specific platform installation geometry, with the baseline length and multipath errors being the key elements dominating GAD systems performance.<sup>[11,13]</sup>

Using multiple antennae suitably positioned in the aircraft, GNSS can provide attitude data. The measurement of the phase of the GNSS signal carrier allows determining the relative displacement of the antennae in the body reference frame.<sup>[5]</sup> VBN techniques use optical sensors (visual or infrared cameras) to extract visual features from images which are then used for localization in the surrounding environment. Cameras have evolved as attractive sensors as they help design economically viable systems with simpler hardware and software components. A number of effective algorithms for VBN system processing have been developed and put to use in the domain of UAVs. Considerable work has been made over the past decade in the area of vision-based techniques for navigation and control.<sup>[14]</sup> Vision-based sensors can also be used to augment GNSS and inertial navigation systems. For this, attitude can be estimated using different techniques such as the sky/ground segmentation<sup>[15]</sup> and color-based separation methods<sup>[16]</sup>. Vision-based methods for navigation gather Simultaneous Localization and Mapping (SLAM)<sup>[17]</sup>, terrain-based navigation and navigation based on feature recognition<sup>[18]</sup>. UAV vision-based systems have been developed for various applications ranging from autonomous landing to obstacle avoidance. Other applications looked into the possible INS and GPS/INS augmentation by using VBN measurements.<sup>[3]</sup> Though several VBN sensors and techniques have been developed to date, the vast majority of VBN sensor schemes fall into one of the following two categories: Model-based Approach (MBA) and Appearance-based Approach (ABA).<sup>[19]</sup> MBA uses feature tracking in images and creates a Three-Dimensional (3D) model of the workspace in which the UAV operates. MBA has been extensively researched in the past and is the most common technique currently implemented for vision-based navigation. The ABA approach has a disadvantage that it requires a large amount of memory to store images and is computationally more costly than MBA. However, due to improvements in computer technology, this technique has become a viable solution in many application areas. We selected the ABA approach for the design of our VBN sensor system. The Image Processing Module (IPM) of the VBN system detects horizon and runway centreline from the images and computes the aircraft attitude, body rates and deviation from the runway centreline. Fig. 2 shows the functional architecture of the IPM.

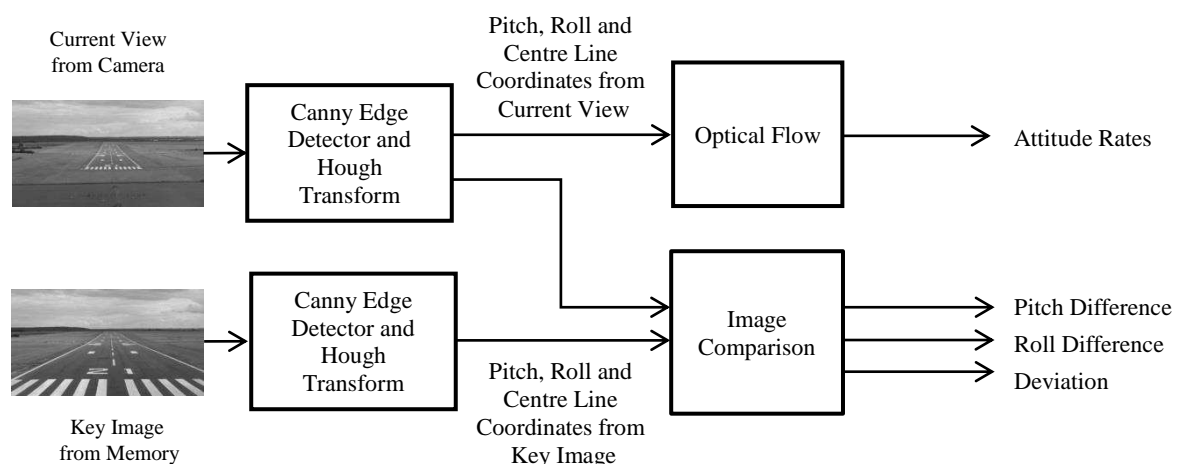


**Fig. 2: Functional architecture of the IPM. Adapted from [4]**

The ADM is used to obtain position, velocity and attitude data. The ADM Virtual Sensor is essentially a Knowledge-Based Module (KBM), which is used to augment the navigation state vector by predicting the UAV flight dynamics (aircraft trajectory and attitude motion). The ADM can employ either a 6DOF or a 3DOF variable mass model with suitable controls and constraints applied in the different phases of the UAV flight. The input data required to run these models are made available from aircraft physical sensors (i.e., aircraft data network stream) and from ad-hoc databases.<sup>[4]</sup>

### 3. MULTI-SENSOR DATA FUSION

GNSS, MEMS-based INS and VBN sensors are utilised for data fusion. Position, velocity and attitude measurements are obtained from GNSS. MEMS-based INS provides position and velocity data while attitude measurements are also obtained both from INS and VBN sensors. ADM, acting as a virtual sensor, also provides attitude measurements. The data provided by all sensors are blended using an EKF. A loosely coupled integration method is implemented in this research. This approach supports the integration of Commercial Off-The-Shelf (COTS) and low-cost navigation sensors.<sup>[20]</sup>

The EKF measurement model is defined as:

$$z(t) = H(t) * x(t) + v(t) \quad (1)$$

where:

$z(t)$  is the measurement (or observation) vector at time  $t$

$x(t)$  is the state vector at time  $t$

$H(t)$  is the design matrix at time  $t$

$v(t)$  is the measurement noise at time  $t$

The process model is described by:

$$\dot{x}(t) = F(t) * x(t) + G(t) * w(t) \quad (2)$$

where:

$\dot{x}(t)$  is the time derivative of the value considered

$F(t)$  is the dynamic matrix of the system at time  $t$

$G(t)$  is the shaping matrix at time  $t$

$w(t)$  is the process noise at time  $t$

For applications where these equations are non-linear, suitable techniques are used to linearize the model. These algorithms are implemented in discrete-time form for easier implementation on a computer. Hence, Eqs. (1) and (2) become:

$$z_k = H_k * x_k + v_k \quad (3)$$

$$x_{k+1} = \Phi_k * x_k + G_k * w_k \quad (4)$$

where,  $k$  stands for the  $k^{\text{th}}$  epoch,  $t_k$  and  $\Phi_k$  is the state transition matrix from epoch  $k$  to  $k+1$ .

The equations of IMU and ADM are non-linear. Furthermore, GNSS pseudo-ranges and pseudo-range rates are also non-linear. Hence, both process and measurement equations need to be linearized. The linearization is performed about a nominal value,  $x^*(t)$ . Then, the state vector is defined as:

$$x(t) = x^*(t) + \delta x(t) \quad (5)$$

where,  $\delta x(t)$  is a perturbation about the nominal value.

After this procedure, the estimation problem consists in evaluating the perturbation vector which becomes the state of the system. Unlike linearized Kalman filter implementations, where linearization is performed about some a priori known nominal trajectory in state space that does not depend on the measurement data, the EKF approach performs linearization about a nominal trajectory (current mean and covariance) that is constantly updated with the state estimates resulting from the measurement. The EKF algorithm process flow is illustrated in Fig. 3.

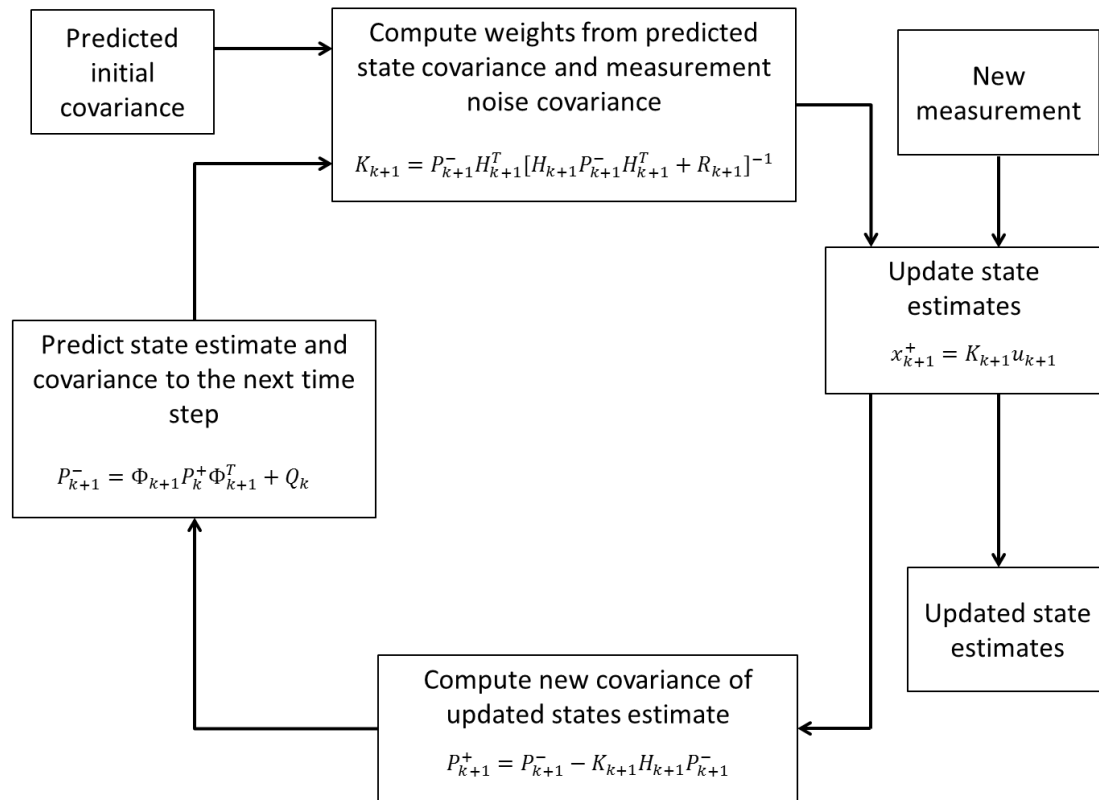


**Fig. 3: Extended Kalman filter algorithm**

The EKF comprises the prediction and the update algorithms. The prediction algorithm estimates the state vector and computes the corresponding covariance matrix  $P_k$  from the current epoch to the next one using the state transition matrix characterizing the process model described by:

$$P_{k+1}^- = \Phi_{k+1} P_k^+ \Phi_{k+1}^T + Q_k \quad (6)$$

where  $P_{k+1}^-$  represents a predicted value computed by the prediction equations and  $P_k^+$  refers to updated values obtained after the correction equations. The process noise at a certain epoch  $k$  is characterized by a covariance matrix,  $Q_k$ . The updating equations correct the predicted state vector and the corresponding covariance matrix using the measurement model as follows:

$$x_{k+1}^+ = K_{k+1} u_{k+1} \quad (7)$$

$$P_{k+1}^+ = P_{k+1}^- - K_{k+1} H_{k+1} P_{k+1}^- \quad (8)$$

where  $K_{k+1}$  is the Kalman gain matrix at epoch,  $k+1$  and  $u_{k+1}$  is the innovation vector at epoch,  $k+1$ . The innovation vector represents the difference between the current measurement and the predicted measurement and can be described as:

$$u_{k+1} = z_{k+1} - H_{k+1}x_{k+1}^- \quad (9)$$

The Kalman gain is used to quantify the influence of new information present in the innovation vector on the estimation of the state vector. It can be considered as a weight factor. It is basically equal to the ratio of the uncertainty on the current measurement and the uncertainty on the predicted one. This gain is defined by:

$$K_{k+1} = P_{k+1}^- H_{k+1}^T [H_{k+1} P_{k+1}^- H_{k+1}^T + R_{k+1}]^{-1} \quad (10)$$

where,  $R_{k+1}$  is the measurement noise covariance matrix.

For the process model defined here, the state vector of the system composed of error in position,  $\delta r^n$ , velocity,  $\delta v^n$  and attitude,  $\epsilon^n$  is described by:

$$x = \begin{bmatrix} \delta r^n \\ \delta v^n \\ \epsilon^n \end{bmatrix} \quad (11)$$

The dynamic matrix of the system is expressed by:

$$F = \begin{bmatrix} F_{rr} & F_{rv} & 0 \\ F_{vr} & F_{vv} & (f^n \times) \\ F_{er} & F_{ev} & -(\delta \omega_{in}^n \times) \end{bmatrix} \quad (12)$$

where,

$$(f^n \times) = \begin{bmatrix} 0 & -e_D & e_E \\ e_D & 0 & -e_N \\ -e_E & e_N & 0 \end{bmatrix} \quad (13)$$

$e_D$  is the yaw error,  $e_N$  is the roll error,  $f^n$  is the specific force transformation matrix from the inertial frame to the navigation frame and

$$-(\delta \omega_{in}^n \times) = \begin{bmatrix} 0 & \omega_e \sin(\phi) + \frac{v_E * \tan \phi}{r_T + h} & \frac{v_N}{r_M + h} \\ -\omega_e \sin(\phi) - \frac{v_E * \tan \phi}{r_T + h} & 0 & \omega_e \cos(\phi) + \frac{v_E}{r_T + h} \\ \frac{-v_N}{r_M + h} & -\omega_e \cos(\phi) - \frac{v_E}{r_T + h} & 0 \end{bmatrix} \quad (14)$$

where,  $\omega_i^n$  is the angular rate transformation matrix from inertial frame to navigation frame,  $\phi$  is latitude,  $h$  is the altitude,  $v_E$  is the velocity in east direction,  $v_N$  is the velocity in north direction,  $\omega_e$  is the angular rate error and the radius of Earth is  $R = \sqrt{r_M^2 + r_T^2}$ . The shaping matrix is given by:

$$G = \begin{bmatrix} 0 & 0 \\ C_b^n & 0 \\ 0 & -C_b^n \end{bmatrix} \quad (15)$$

where,  $C_b^n$  is the transformation matrix from the body frame to the navigation frame. The process noise is composed of errors in accelerometers and gyroscopes measurements and is given by:

$$w(t) = \begin{bmatrix} 0 \\ \delta f^b \\ \delta \omega^b \end{bmatrix} \quad (16)$$

The inertial measurement errors do not behave as a zero-mean white Gaussian noise. Hence, the state vector has to be augmented to take into account the effect of the inertial sensor errors. Usually for high-accuracy INS sensors, only the bias drift and noise must be considered. Hence, the errors of accelerometers and gyroscopes are expressed by:

$$\delta f^b = \delta b_a + \eta_a \quad (17)$$

$$\delta \omega^b = \delta b_g + \eta_g \quad (18)$$

where:

$\delta b_a$  and  $\delta b_g$  are the accelerometers and gyroscopes biases,  $\eta_a$  and  $\eta_g$  are the accelerometers and gyroscopes noises, with spectral densities as  $q_a$  and  $q_g$ , respectively.

Following [21], the bias drift can be modeled as a first-order Gauss-Markov process and are given by:

$$\dot{\delta b}_{ai} = -\frac{1}{\tau_{bai}} \delta b_{ai} + \eta_{bai} \quad (19)$$

$$\dot{\delta b}_{gi} = -\frac{1}{\tau_{bgi}} \delta b_{gi} + \eta_{bgi} \quad (20)$$

where:

$i \in \{x, y, z\}$ .  $\tau_{ba}$  and  $\tau_{bg}$  are the correlation times for accelerometers and gyroscopes.  $\eta_{ba}$  and  $\eta_{bg}$  are the Gaussian-Markov process driving noise.  $q_{ba}$  and  $q_{bg}$  are the spectral densities.

The spectral densities are computed using:

$$q_{bai} = \frac{2\sigma_{bai}^2}{\tau_{bai}} \quad (21)$$

$$q_{bgi} = \frac{2\sigma_{bgi}^2}{\tau_{bgi}} \quad (22)$$

where,  $\sigma_{ba}$  and  $\sigma_{bg}$  are the Gauss-Markov process temporal standard deviations ( $\sigma$ ). When using MEMS-based INS, the turn-on bias and the scale factor are typically high and must also be taken into account. The turn on bias can be modeled as a random constant process and is then supposed to be included in the drift bias. Following [22], the scale factor can be modeled as a first-order Gauss-Markov process with large correlation time. Hence, in the



same manner as for the drift bias, the scale factors are expressed as  $\delta S_{ai}$  and  $\delta S_{gi}$  for accelerometers and gyroscopes.  $\tau_{sa}$  and  $\tau_{sg}$  are the correlation times for accelerometers and gyroscopes scale factors.  $\eta_{sa}$  and  $\eta_{bg}$  are the Gaussian-Markov process driving noise.  $q_{sa}$  and  $q_{sg}$  are the spectral densities. Hence, the augmented process model is obtained as follows:

$$\dot{x}(t) = \begin{bmatrix} \delta \dot{r}^n \\ \delta \dot{v}^n \\ \epsilon^n \\ \delta \dot{b}_a \\ \delta \dot{b}_g \\ \delta \dot{S}_a \\ \delta \dot{S}_g \end{bmatrix} = \begin{bmatrix} F_{rr} & F_{rv} & 0_3 & 0_3 & 0_3 & 0_3 & 0_3 \\ F_{vr} & F_{vv} & (f^n \times) & C_b^n & 0_3 & C_b^n F^b & 0_3 \\ F_{er} & F_{ev} & -(\delta \omega_{in}^n \times) & 0_3 & -C_b^n & 0_3 & C_b^n W^b \\ 0_3 & 0_3 & 0_3 & D_{ba} & 0_3 & 0_3 & 0_3 \\ 0_3 & 0_3 & 0_3 & 0_3 & D_{bg} & 0_3 & 0_3 \\ 0_3 & 0_3 & 0_3 & 0_3 & 0_3 & D_{Sa} & 0_3 \\ 0_3 & 0_3 & 0_3 & 0_3 & 0_3 & 0_3 & D_{Sg} \end{bmatrix} \begin{bmatrix} \delta r^n \\ \delta v^n \\ \epsilon^n \\ \delta b_a \\ \delta b_g \\ \delta S_a \\ \delta S_g \end{bmatrix} + \begin{bmatrix} 0_3 & 0_3 & 0_3 & 0_3 & 0_3 & 0_3 & 0_3 \\ C_b^n & 0_3 & 0_3 & 0_3 & 0_3 & 0_3 & 0_3 \\ 0_3 & -C_b^n & 0_3 & 0_3 & 0_3 & 0_3 & 0_3 \\ 0_3 & 0_3 & I_3 & 0_3 & 0_3 & 0_3 & 0_3 \\ 0_3 & 0_3 & 0_3 & I_3 & 0_3 & 0_3 & 0_3 \\ 0_3 & 0_3 & 0_3 & 0_3 & I_3 & 0_3 & 0_3 \\ 0_3 & 0_3 & 0_3 & 0_3 & 0_3 & I_3 & 0_3 \end{bmatrix} \begin{bmatrix} \eta_a \\ \eta_g \\ \eta_{ba} \\ \eta_{bg} \\ \eta_{sa} \\ \eta_{sg} \end{bmatrix} \quad (23)$$

where,

$$D_{ba} = \begin{bmatrix} \frac{-1}{\tau_{bax}} & 0 & 0 \\ 0 & \frac{-1}{\tau_{bay}} & 0 \\ 0 & 0 & \frac{-1}{\tau_{baz}} \end{bmatrix} \text{ and } D_{bg} = \begin{bmatrix} \frac{-1}{\tau_{bgx}} & 0 & 0 \\ 0 & \frac{-1}{\tau_{bgy}} & 0 \\ 0 & 0 & \frac{-1}{\tau_{bgz}} \end{bmatrix}$$

$$D_{Sa} = \begin{bmatrix} \frac{-1}{\tau_{Sax}} & 0 & 0 \\ 0 & \frac{-1}{\tau_{Say}} & 0 \\ 0 & 0 & \frac{-1}{\tau_{Saz}} \end{bmatrix} \text{ and } D_{Sg} = \begin{bmatrix} \frac{-1}{\tau_{Sgx}} & 0 & 0 \\ 0 & \frac{-1}{\tau_{Sgy}} & 0 \\ 0 & 0 & \frac{-1}{\tau_{Sgz}} \end{bmatrix} \quad (24)$$

$$F^b = \begin{bmatrix} f_x & 0 & 0 \\ 0 & f_y & 0 \\ 0 & 0 & f_z \end{bmatrix} \text{ and } W^b = \begin{bmatrix} \omega_x & 0 & 0 \\ 0 & \omega_y & 0 \\ 0 & 0 & \omega_z \end{bmatrix}$$

The covariance matrix of the model is given by:

$$Q = \begin{bmatrix} q_a & 0 & 0 & 0 & 0 & 0 \\ 0 & q_g & 0 & 0 & 0 & 0 \\ 0 & 0 & q_{ba} & 0 & 0 & 0 \\ 0 & 0 & 0 & q_{bg} & 0 & 0 \\ 0 & 0 & 0 & 0 & q_{sa} & 0 \\ 0 & 0 & 0 & 0 & 0 & q_{sg} \end{bmatrix} \quad (25)$$

The discrete process noise matrix is defined as follows:

$$Q_k \sim G(t_k)Q(t_k)G^T(t_k) \quad (26)$$

When the position errors are expressed in radians (latitude and longitude), the values can be so meager that they can lead to numerical instabilities in the Kalman filter.<sup>[23]</sup> Then it is preferable to express them in NED coordinates.<sup>[24]</sup> For this, the position terms in the state vector  $x(t)$  in Eq. (2) are transformed. Defining  $x'$  as the new state error vector, after being transformed by the matrix  $T$ , we obtain:

$$x' = Tx \quad (27)$$

$$x = T^{-1}x' \quad (28)$$

Substituting Eqs. (27) and (28) in Eq. (2), we obtain:

$$\dot{x}' = \dot{T}x + T\dot{x} = \dot{T}T^{-1}x' + TFx + TGw = (\dot{T}T^{-1} + TFT^{-1})x' + TGw \quad (29)$$

$$\dot{x}' = F'x' + G'w \quad (30)$$

where,  $F'$  and  $G'$  are the new dynamics and shaping matrices defined by:

$$F' = \dot{T}T^{-1} + TFT^{-1} \approx TFT^{-1} \quad (31)$$

$$G' = TG \quad (32)$$

Herein, the state error vector  $x$  with position error  $\delta r^n$  expressed in terms of latitude and longitude (radians) is transformed into  $x'$  with position error  $\delta P^n$  expressed in meters as:

$$x = \begin{bmatrix} \delta r^n \\ \delta v^n \\ \epsilon^n \\ \delta b_a \\ \delta b_g \\ \delta S_a \\ \delta S_g \end{bmatrix}; \quad x' = \begin{bmatrix} \delta P^n \\ (\delta v^n)' \\ (\epsilon^n)' \\ (\delta b_a)' \\ (\delta b_g)' \\ (\delta S_a)' \\ (\delta S_g)' \end{bmatrix} \quad (33)$$

where,  $\delta P^n$  is the position error state,  $\delta v^n$  is the velocity error,  $\epsilon^n$  is the attitude error term, and

$$\delta P^n = [\delta N \quad \delta E \quad \delta D]^T \quad (34)$$

The transition matrix to pass from the previous state error vector to the new one is  $T$  and is given by:

$$T = \begin{bmatrix} A & 0_{18 \times 18} \\ 0_{18 \times 18} & I_{18} \end{bmatrix} \quad (35)$$

$$A = \begin{bmatrix} r_M + h & 0 & 0 \\ 0 & (r_T + h)\cos(\varphi) & 0 \\ 0 & 0 & -1 \end{bmatrix} \quad (36)$$

The process model with the new position error state is:

$$\begin{bmatrix} \delta \dot{P}^n \\ \delta \dot{V}^n \\ \epsilon^n \\ \delta \dot{b}_a \\ \delta \dot{b}_g \\ \delta \dot{S}_a \\ \delta \dot{S}_g \end{bmatrix} = \begin{bmatrix} F_{PP} & F_{PV} & 0_3 & 0_3 & 0_3 & 0_3 & 0_3 \\ F_{VP} & F_{VV} & (f^n \times) & C_b^n & 0_3 & C_b^n F^b & 0_3 \\ F_{eP} & F_{ev} & -(\delta \omega_{in}^n \times) & 0_3 & -C_b^n & 0_3 & C_b^n W^b \\ 0_3 & 0_3 & 0_3 & D_{ba} & 0_3 & 0_3 & 0_3 \\ 0_3 & 0_3 & 0_3 & 0_3 & D_{bg} & 0_3 & 0_3 \\ 0_3 & 0_3 & 0_3 & 0_3 & 0_3 & D_{Sa} & 0_3 \\ 0_3 & 0_3 & 0_3 & 0_3 & 0_3 & 0_3 & D_{Sg} \end{bmatrix} * \begin{bmatrix} \delta P^n \\ \delta V^n \\ \epsilon^n \\ \delta b_a \\ \delta b_g \\ \delta S_a \\ \delta S_g \end{bmatrix} + \begin{bmatrix} 0_3 & 0_3 & 0_3 & 0_3 & 0_3 & 0_3 \\ C_b^n & 0_3 & 0_3 & 0_3 & 0_3 & 0_3 \\ 0_3 & -C_b^n & 0_3 & 0_3 & 0_3 & 0_3 \\ 0_3 & 0_3 & I_3 & 0_3 & 0_3 & 0_3 \\ 0_3 & 0_3 & 0_3 & I_3 & 0_3 & 0_3 \\ 0_3 & 0_3 & 0_3 & 0_3 & I_3 & 0_3 \\ 0_3 & 0_3 & 0_3 & 0_3 & 0_3 & I_3 \end{bmatrix} * \begin{bmatrix} \eta_a \\ \eta_g \\ \eta_{ba} \\ \eta_{bg} \\ \eta_{Sa} \\ \eta_{Sg} \end{bmatrix} \quad (37)$$

As the matrices  $F_{rr}$ ,  $F_{rv}$ ,  $F_{vr}$  and  $F_{er}$  are related to position information, they must be modified in concordance with the change in position reference. The new values of these matrices are given by the following equations:

$$F_{PP} = T F_{rr} T^{-1} \quad (38)$$

$$F_{PV} = T F_{rv} T^{-1} \quad (39)$$

$$F_{VP} = T F_{vr} T^{-1} \quad (40)$$

$$F_{eP} = T F_{er} T^{-1} \quad (41)$$

For the measurement model, the observation equation has the following discrete form:

$$z_k = H_k x_k + v_k \quad (42)$$

As three different sensors can be used for Position, Velocity and Attitude (PVA) computations, different integration modes are implemented and simulated.

#### 4. MULTISENSOR SYSTEM DESIGN AND SIMULATION

Three different integrated navigation system architectures were defined, including VBN/IMU/GPS (VIG), VIG/ADM (VIGA) and the VIG/GAD (VIGGA). The VIG architecture uses VBN at 20 Hz and GPS at 1 Hz to augment the MEMS-IMU running at 100 Hz. The VIGA architecture includes the ADM (computations performed at 100 Hz) to provide attitude channel augmentation, while the VIGGA architecture includes GNSS to provide attitude channel augmentation. The corresponding VIG, VIGA and VIGGA integrated navigation modes were simulated using MATLAB™ covering all relevant flight phases of an AEROSONDE UAV (straight climb, straight-and-level flight, level turn, climb/descend turn, straight descent, etc.). The navigation system outputs were fed to a hybrid Fuzzy-logic/PID controller designed for the AEROSONDE UAV and capable of operating with stand-alone VBN, as well as with other sensors data.<sup>[4,6]</sup>

##### 4.1 VIG, VIGA and VIGGA Architectures

The VIG architecture is illustrated in Fig. 4. The INS provides measurements from gyroscopes and accelerometers which are fed to a navigation processor. GNSS provides raw pseudorange measurements which are processed by a filter to obtain position and velocity data.

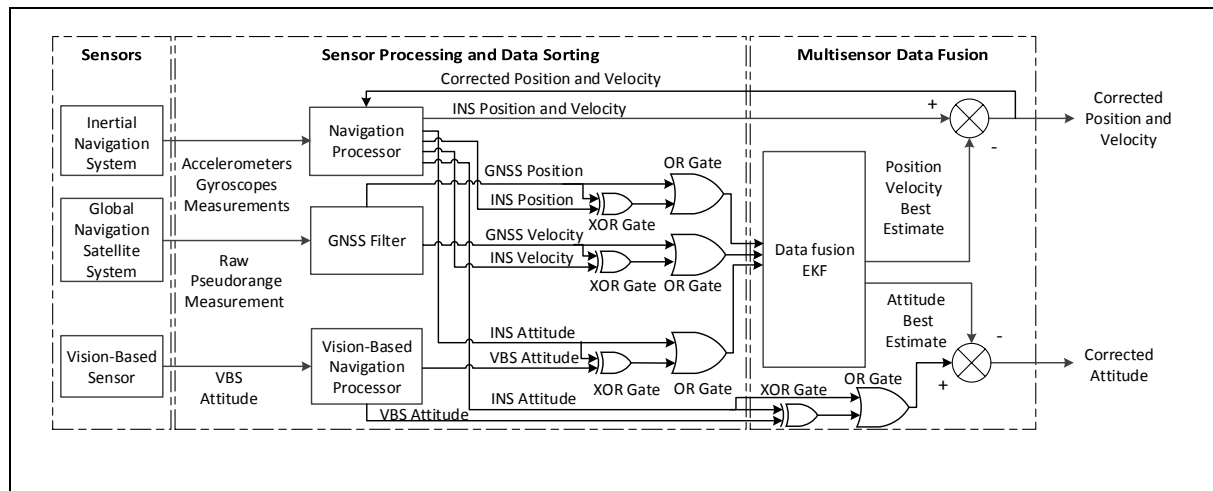


**Fig. 4: VIG architecture**

In the VIG system, the INS position and velocity provided by the navigation processor are compared to the GNSS position and velocity to form the measurement input of the data fusion block containing the EKF. A similar process is also applied to the INS and VBN attitude angles, whose differences are incorporated in the EKF measurement vector. The EKF provides estimates of the PVA errors, which are then removed from the sensor measurements to obtain the corrected PVA states. The corrected PVA and estimates of accelerometer and gyroscope biases are also used to update the INS raw measurements. The VIGA architecture is illustrated in Fig. 5. As before, the INS position and velocity provided by the navigation processor are compared to the GNSS data to form the measurement input of EKF.

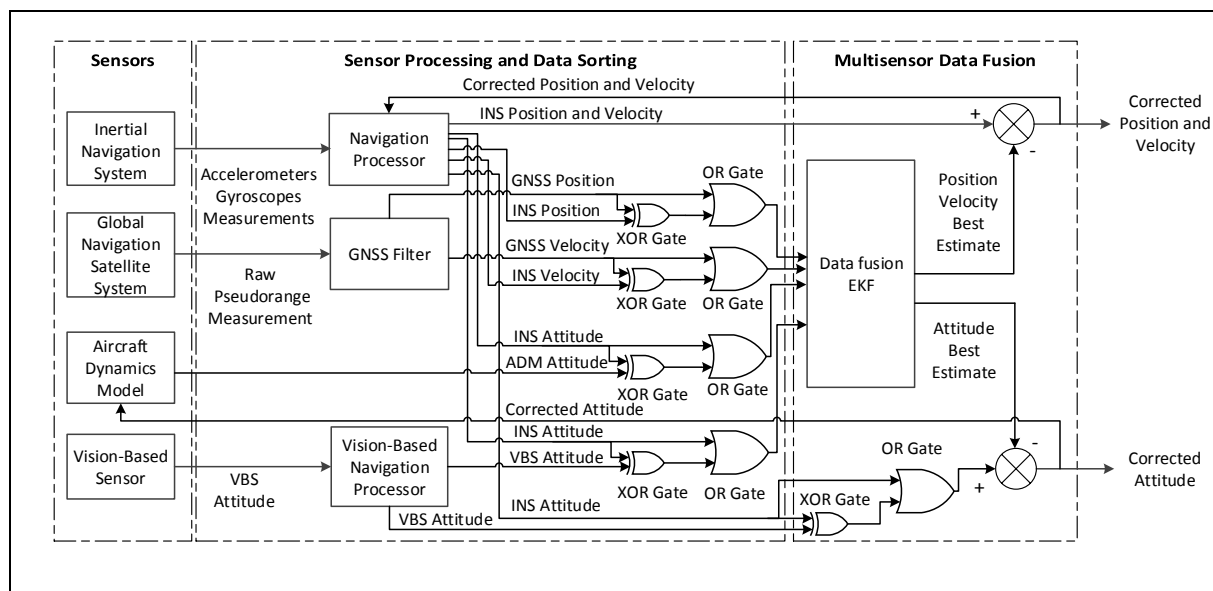


**Fig. 5: VIGA architecture**

Additionally, in this case, the attitude data provided by the ADM and the INS are compared to feed the EKF at 100 Hz, and the attitude data provided by the Vision Based Sensors (VBS) and INS are compared at 20 Hz and input to the EKF (Fig. 5). Like in the VIG architecture, the EKF provides estimations of PVA errors, which are removed from the INS measurements to obtain the corrected PVA states. Again, the corrected PVA and estimates of accelerometer and gyroscope biases are used to update INS raw measurements. The

attitude best estimate is compared with the INS attitude to obtain the corrected attitude. During the landing phase, the attitude best estimate is compared with the VBS attitude to obtain the corrected attitude. Then, the GNSS attitude determination is integrated to the VIG Navigation System to form the VIGGA architecture, as illustrated in Fig. 6. In addition to the VIG architecture, the raw carrier-phase measurement is used for GAD system (GADS) to provide GADS attitude. The attitudes from INS, VBS and GADS form the attitude measurement inputs for the data fusion block. In this case, the corrected PVA and estimates of accelerometer and gyroscope biases are used to update INS raw measurements.

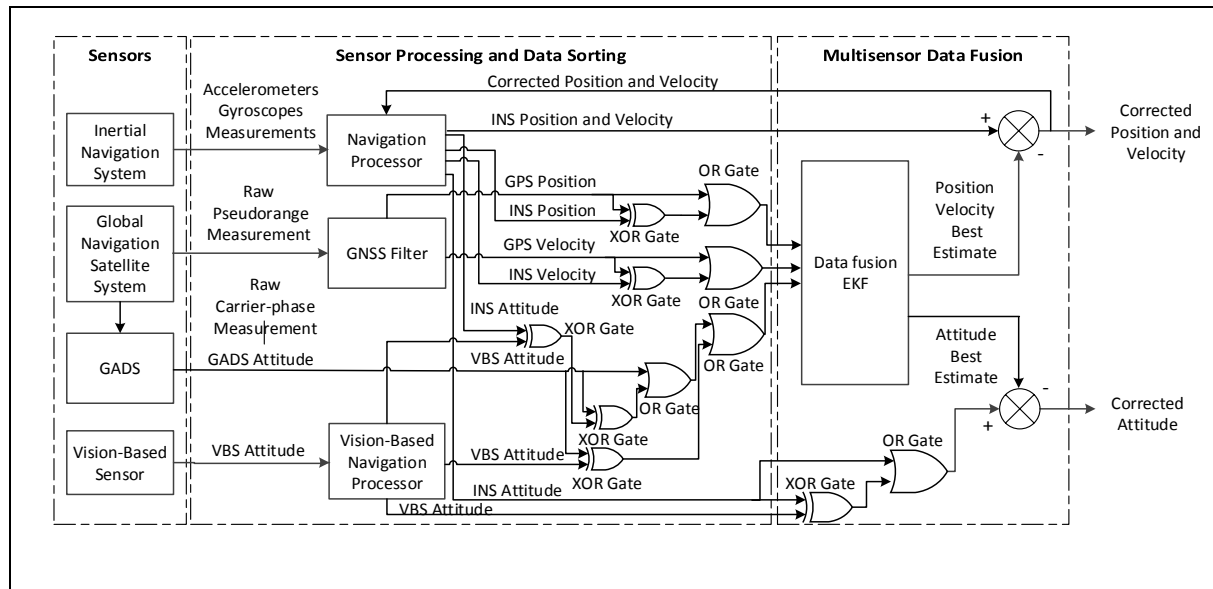


Fig. 6: VIGGA architecture

In our research, INS-MEMS errors are modeled as White Noise (WN) or Gauss-Markov (GM) processes. Table 1 lists the MEMS-INS error parameters considered in our research.

Table 1: MEMS-INS error parameters. Adapted from [4]

IMU Error Parameters	Error Models
p gyro noise	WN (0.53 $^{\circ}$ /s)
q gyro noise	WN (0.45 $^{\circ}$ /s)
r gyro noise	WN (0.44 $^{\circ}$ /s)
x accelerometer noise	WN (0.013 $\text{m/s}^2$ )
y accelerometer noise	WN (0.018 $\text{m/s}^2$ )
z accelerometer noise	WN (0.010 $\text{m/s}^2$ )
p gyro bias	GM (0.0552 $^{\circ}$ /s, 300 s)
q gyro bias	GM (0.0552 $^{\circ}$ /s, 300 s)
r gyro bias	GM (0.0552 $^{\circ}$ /s, 300 s)
x accelerometer bias	GM (0.0124 $\text{m/s}^2$ , 300 s)
y accelerometer bias	GM (0.0124 $\text{m/s}^2$ , 300 s)
z accelerometer bias	GM (0.0124 $\text{m/s}^2$ , 300 s)
p gyro scale factor	GM (10000 PPM, 18000 s)
q gyro scale factor	GM (10000 PPM, 18000 s)
r gyro scale factor	GM (10000 PPM, 18000 s)
x accelerometer scale factor	GM (10000 PPM, 18000 s)
y accelerometer scale factor	GM (10000 PPM, 18000 s)
z accelerometer scale factor	GM (10000 PPM, 18000 s)

Table 2 lists the position and velocity error statistics of state-of-the-art SPS GPS receivers. Typically, GPS position and velocity measurements are provided at a rate of 1 Hz.

**Table 2: GPS position and velocity errors. Adapted from [4]**

Errors	Mean	$\sigma$
North Position Error (m)	-0.4	1.79
East Position Error (m)	0.5	1.82
Down Position Error (m)	0.17	3.11
North Velocity Error (mm/s)	0	3.8
East Velocity Error (mm/s)	0	2.9
Down Velocity Error (mm/s)	2.9	6.7

Employing a geometric algorithm for optimal selection of the antenna baselines and recursive algorithm for over-determined attitude computations,<sup>[5]</sup> the resulting error statistics are presented in Table 3, which are utilised in the GAD system design.

**Table 3: GNSS attitude determination errors. Adapted from [5]**

Configuration	1- $\sigma$ Pitch Error (°)	1- $\sigma$ Roll Error (°)	1- $\sigma$ Yaw Error (°)
3 Antennae	1.37	0.93	1.77
4 Antennae	0.47	0.32	0.76
5 Antennae	0.38	0.52	0.54

## 5. VIG, VIGA AND VIGGA SIMULATION

The AEROSONDE model used for simulation is from Unmanned Dynamics LLC. The AEROSONDE UAV is a small autonomous aircraft used in weather-reconnaissance and remote-sensing missions. Its main characteristics are listed in Fig. 7.

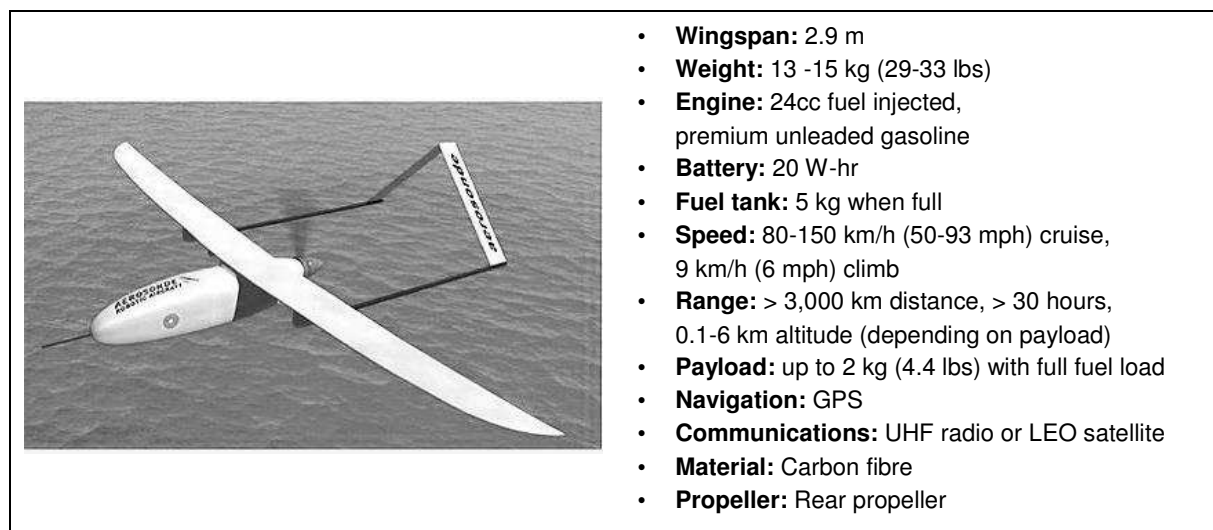


**Fig. 7: AEROSONDE UAV characteristics. Adapted from [25]**

An AEROSONDE dynamics model is implemented in MATLAB/Simulink utilising the AeroSim blockset.<sup>[26]</sup> This blockset provides components for rapid development of non-linear

6DOF dynamic models. In addition to the basic dynamic blocks, complete aircraft models are present which can be configured as required. The library also includes Earth models (geoid references, gravity and magnetic fields) and atmospheric models. The AEROSONDE UAV model can be interfaced with simulators such as Flight-Gear and Microsoft™ Flight Simulator to allow visualisation of the aircraft trajectory. The inputs to the AEROSONDE model include control surface deflections in radians, throttle input, mixture and ignition. Wind disturbances can be added to the model to simulate variable atmospheric conditions. The various aircraft states such as the position in the Earth-fixed frame, attitude and attitude rates can be obtained as outputs from the model.

In order to perform the GNSS attitude determination for the AEROSONDE, a configuration comprising 5 GNSS antennae was selected to optimize the length of the baselines in various dynamics conditions.<sup>[27]</sup> The baseline lengths for all antennae combinations are listed in Table 4.

**Table 4: Baseline lengths (cm) of antennae in the AEROSONDE UAV**

Antennae	1	2	3	4	5
1		100	180	120	200
2	100		100	100	140
3	180	100		100	100
4	120	100	100		130
5	200	140	100	130	

The position of the antennae in the AEROSONDE UAV can be observed in Fig. 8.

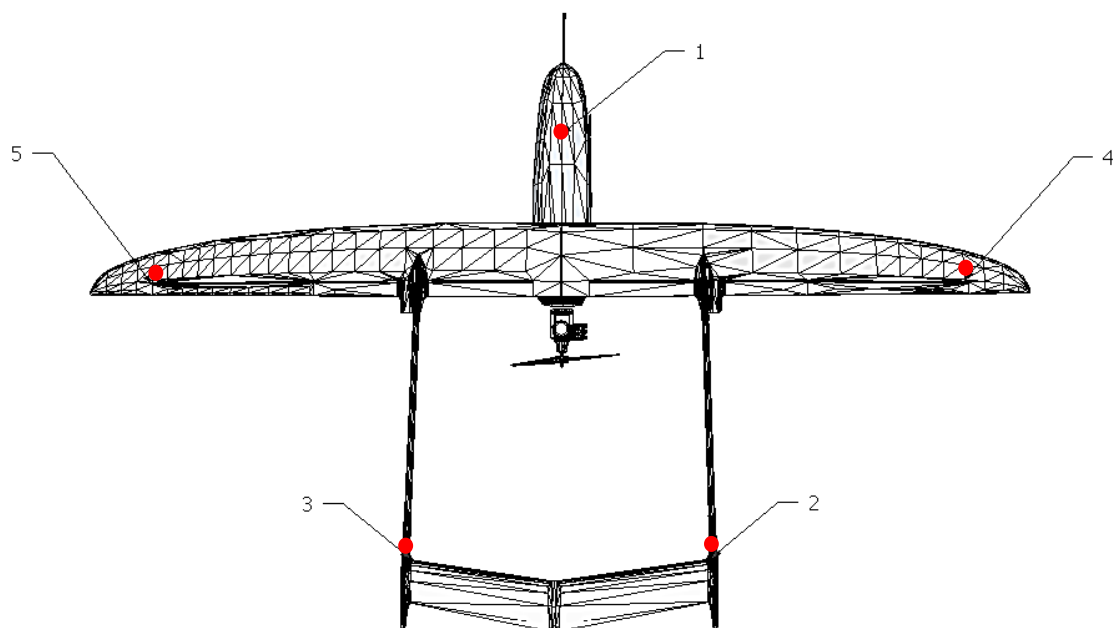


**Fig. 8: Proposed antennae locations. Adapted from [25]**

The VIG, VIGA and VIGGA multi-sensor architectures were tested by simulation in an appropriate sequence of high dynamics flight manoeuvres representative of the AEROSONDE UAV operational flight envelope. Case studies considering low dynamics were presented in previous work.<sup>[4-6]</sup> A hybrid Fuzzy/PID controller was used for the

simulation. The duration of the simulation is 900 s (15 min). The 3D trajectory plot of the flight phases followed by the AEROSONDE UAV is shown in Fig. 9.

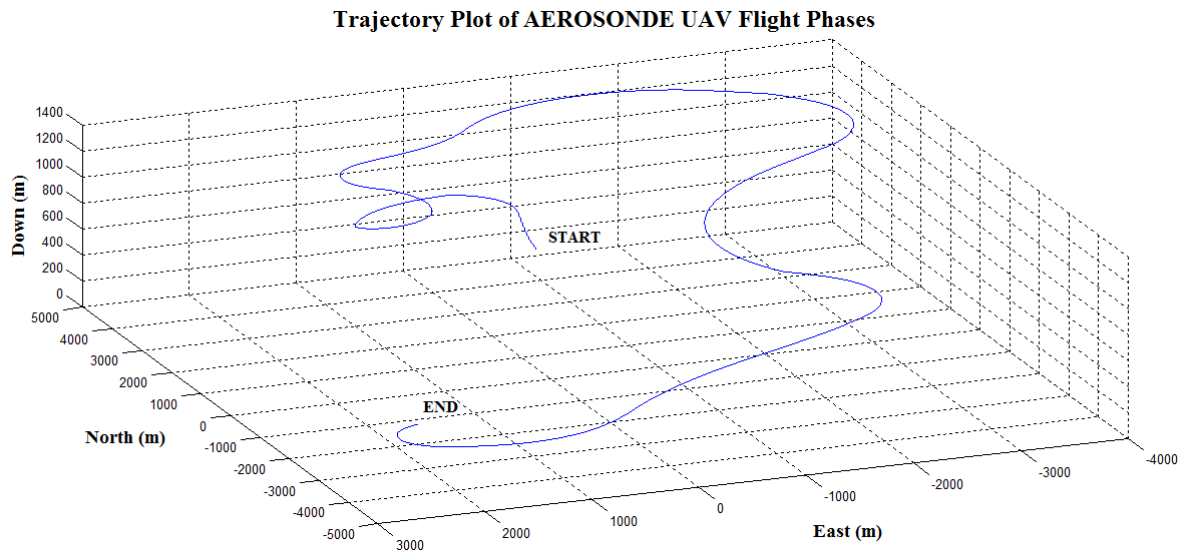


**Fig. 9: 3D trajectory plot of the AEROSONDE UAV flight phases**

The list of simulated flight manoeuvres and associated control inputs is provided in Table 5.

**Table 5: Flight manoeuvres and control inputs**

Flight Maneuver	Required Roll (°)	Required Pitch (°)	Time (s)
Straight Climb (Take-off)	0	10	50
Left Turning Climb	5	10	50
Straight Climb	4	2	50
Left Turning Climb	8	10	50
Left Turning Climb	3	5	50
Right Turning Climb	-7	2	50
Level Left Turn	3	2.5	50
Right Turning Climb	-3	2.25	50
Straight and Level	0	2.1	100
Right Turning Descent	-6	-2	30
Left Turning Descent	5	-6	70
Level Right Turn	-6	-1	100
Straight Descent	0	-5	70
Left Turning Descent	3	-5	30
Right Turning Descent	-7	0	50
Straight Descent	-10	-2	50

The position error time histories of the VIG system are shown in Figs. 10-12 and the comparison of error time histories in GPS position and estimated position is shown in Figs. 13-15. Table 6 presents the associated position error statistics.



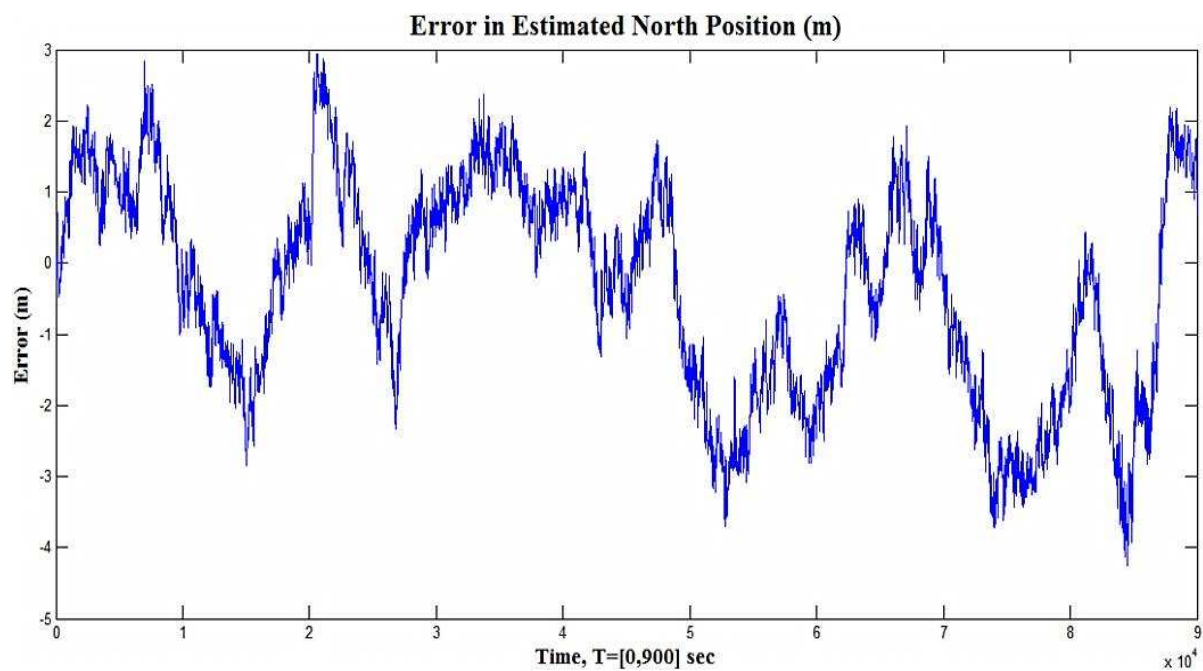


**Fig. 10: VIG position error time histories (North Position)**

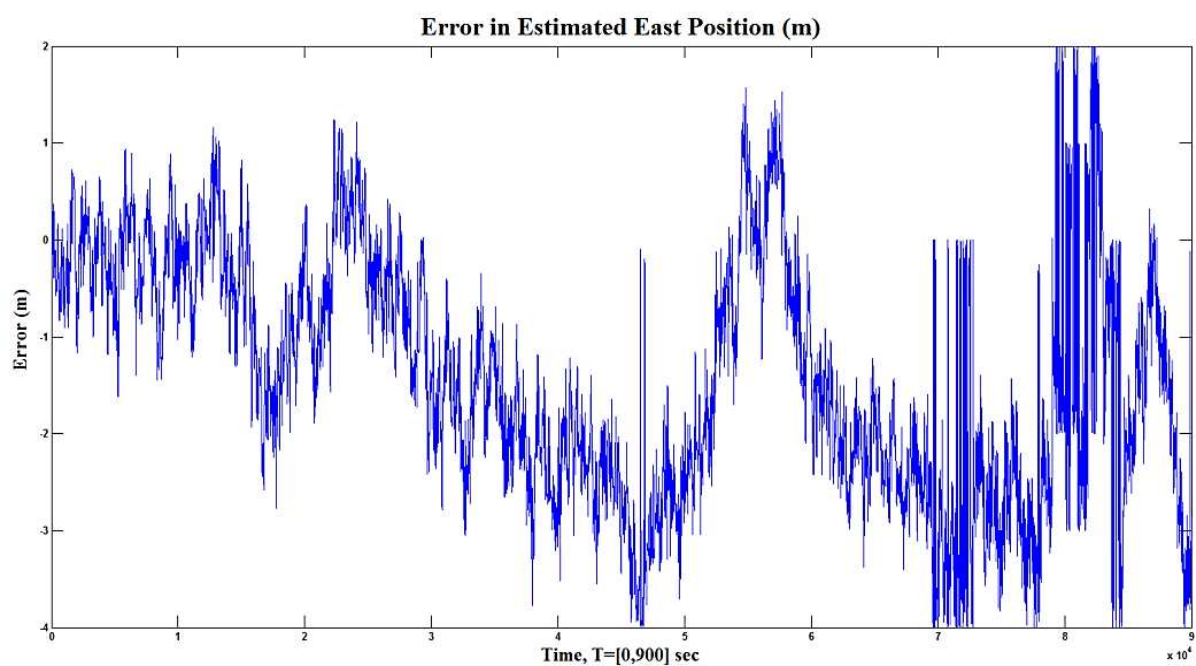


**Fig. 11: VIG position error time histories (East Position)**

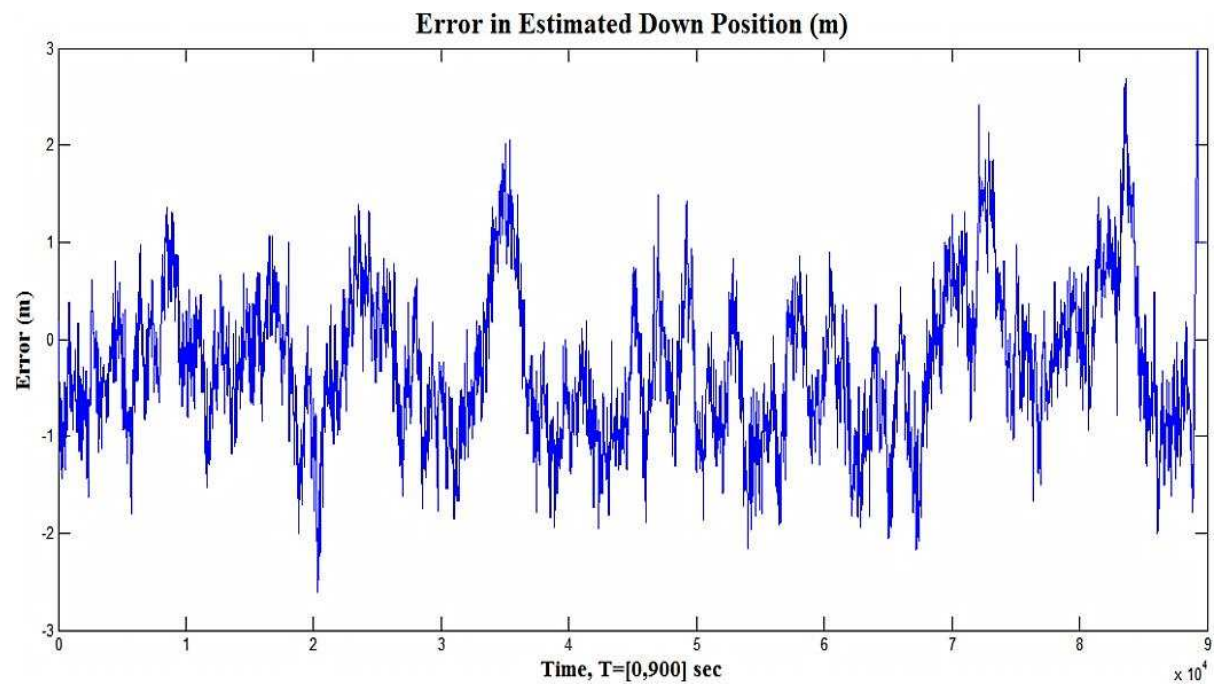


**Fig. 12: VIG position error time histories (Down Position)**

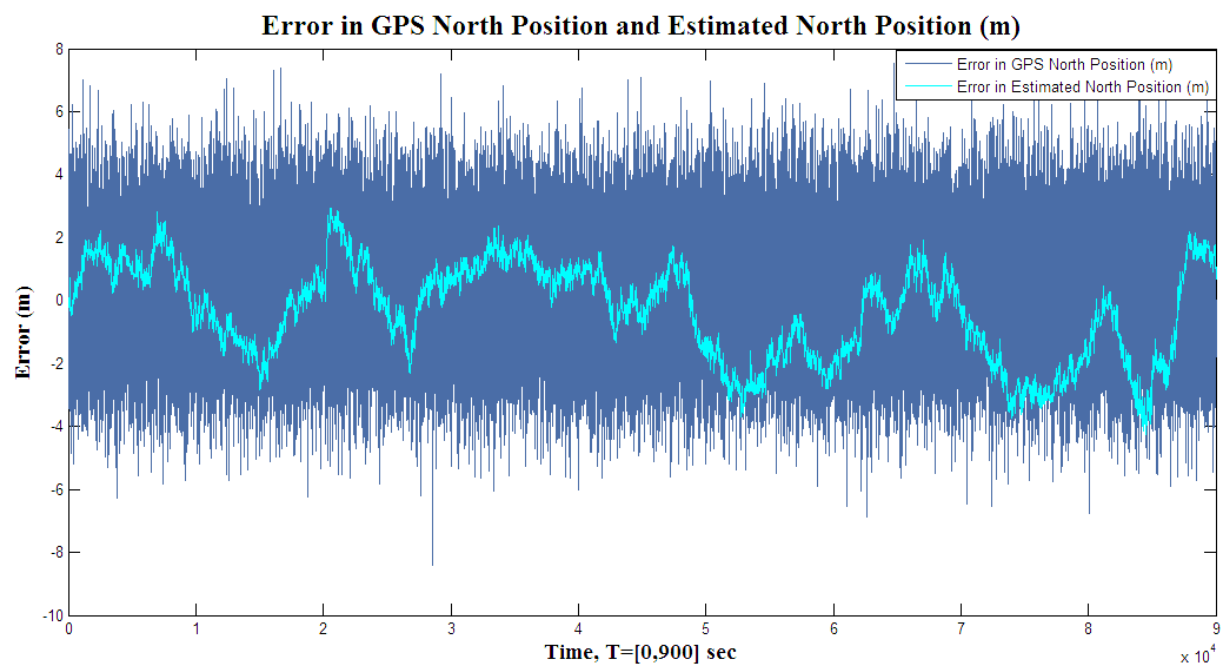


**Fig. 13: Comparison of GPS and estimated error time histories (North Position)**

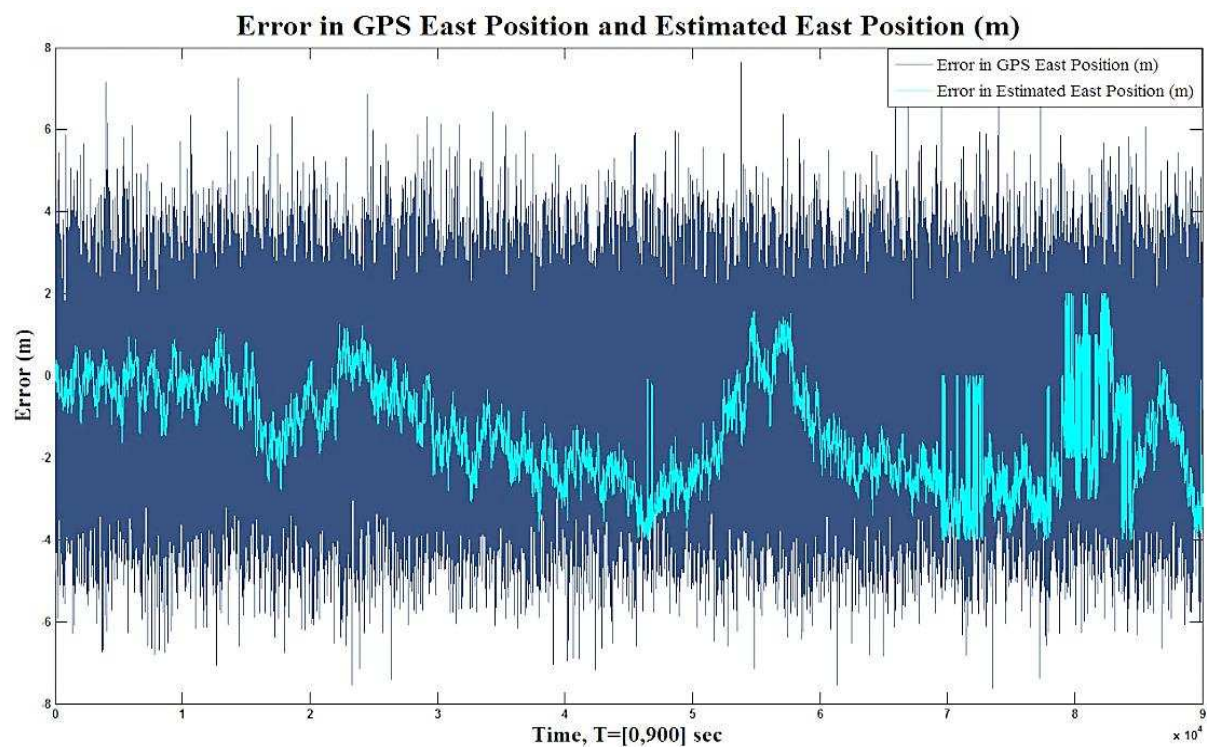


**Fig. 14: Comparison of GPS and estimated error time histories (East Position)**

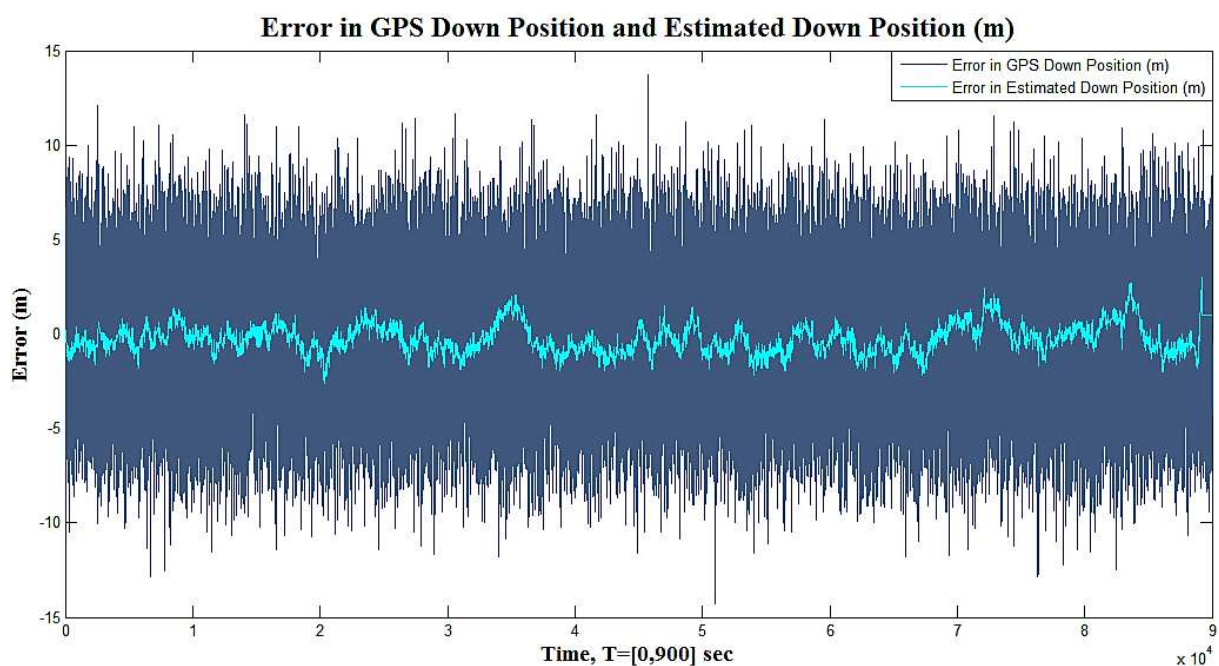


**Fig. 15: Comparison of GPS and estimated error time histories (Down Position)**

**Table 6 : VIG position error statistics**

Phase of Flight	North Position		East Position		Down Position	
	Mean (m)	$\sigma$ (m)	Mean (m)	$\sigma$ (m)	Mean (m)	$\sigma$ (m)
<b>Straight Climb (Take-off)</b>	1.1083	0.5898	-0.1871	0.3950	-0.4323	0.4526
<b>Left Turning Climb</b>	1.0531	0.7402	-0.2290	0.5290	-0.0061	0.6279
<b>Straight Climb</b>	-1.0103	0.5750	-0.1440	0.4886	-0.2847	0.4418
<b>Left Turning Climb</b>	-0.5439	0.9859	-1.1443	0.6512	-0.2370	0.6316
<b>Left Turning Climb</b>	1.2762	0.9123	-0.1795	0.7266	-0.1668	0.8227
<b>Right Turning Climb</b>	-0.2348	0.8295	-0.7101	0.5436	-0.3723	0.5814
<b>Level Left Turn</b>	1.2218	0.4054	-1.6185	0.5150	-0.2319	0.9198
<b>Right Turning Climb</b>	0.9858	0.4464	-2.1581	0.5243	-0.3121	0.8973
<b>Straight and Level</b>	0.1833	0.7959	-2.6409	0.5857	-0.4924	0.6470
<b>Right Turning Descent</b>	-2.2828	0.6284	-1.8643	0.6274	-0.6582	0.5355
<b>Left Turning Descent</b>	-1.9248	0.6540	-0.1079	0.7832	-0.6508	0.6241
<b>Level Right Turn</b>	-0.0994	0.9621	-2.2339	0.5659	-0.5571	0.6931
<b>Straight Descent</b>	-2.2297	0.9138	-3.0027	0.6428	0.3077	0.7733
<b>Left Turning Descent</b>	-2.3176	0.4634	-3.1809	0.6781	-0.0204	0.3746
<b>Right Turning Descent</b>	-1.6805	1.2577	-4.0724	0.8570	0.6399	0.7663
<b>Straight Descent</b>	0.0800	1.6687	-1.7419	1.0068	-0.4066	0.8959
<b>All Phases</b>	-0.3419	1.5057	-1.6287	1.3603	-0.2665	0.7715

As discussed above, the ADM data were used in the VIGA architecture to update the attitude channel (the position and velocity channels are derived from the VIG system). The time histories of the VIGA attitude errors are shown in Figs. 16-18 and compared with the corresponding VIG attitude errors. Table 7 presents the attitude error statistics for the VIGA system. Figs. 19-21 illustrate the error comparison of the attitude errors obtained from VIGGA (3 antennae configuration) with the results obtained from the VIG system. Table 8 presents the attitude error statistics for the VIGGA system.

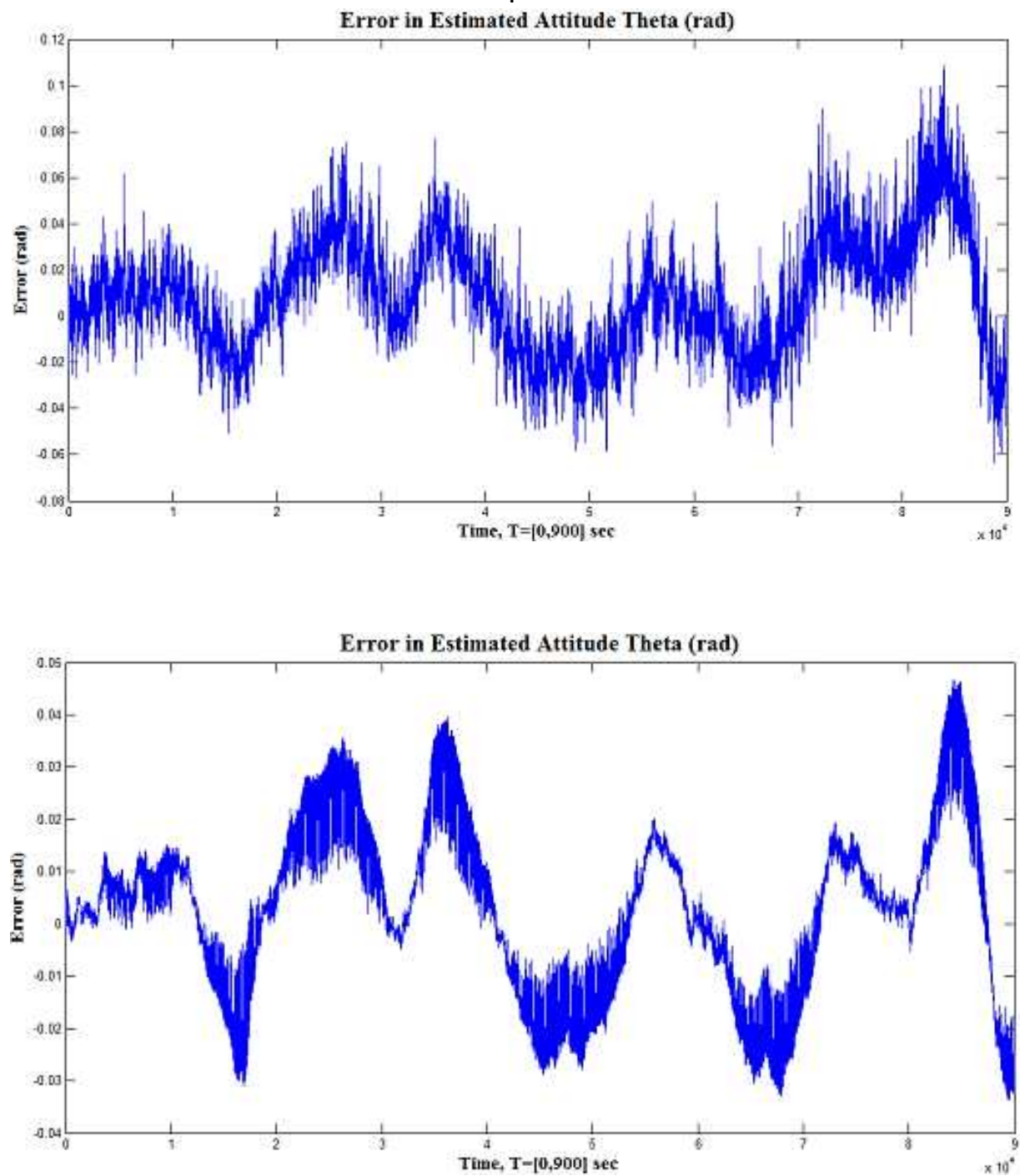


Fig. 16: Comparison of VIG (top) and VIGA (bottom) attitude errors (Theta)



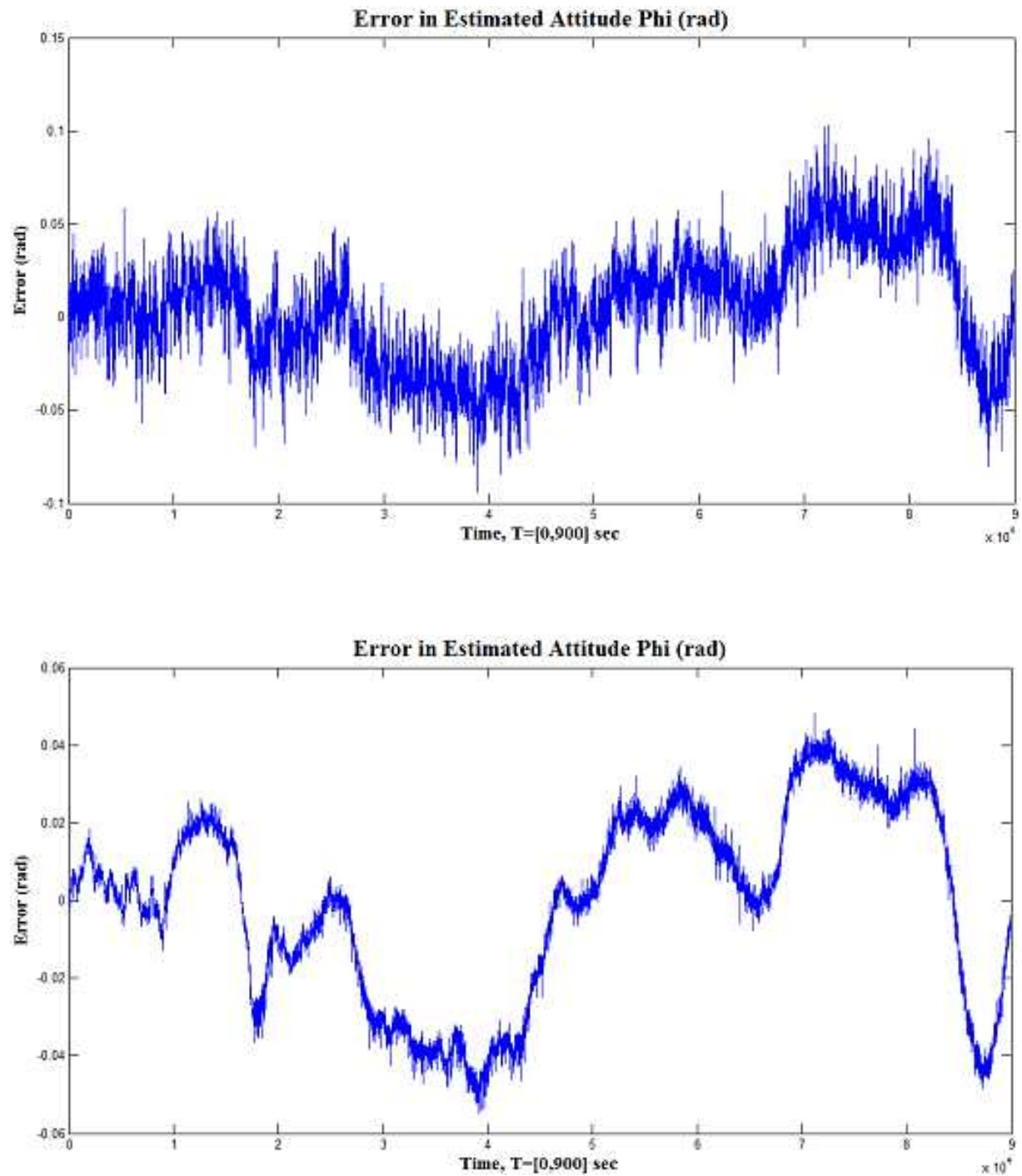


Fig. 17: Comparison of VIG (top) and VIGA (bottom) attitude errors (Phi)

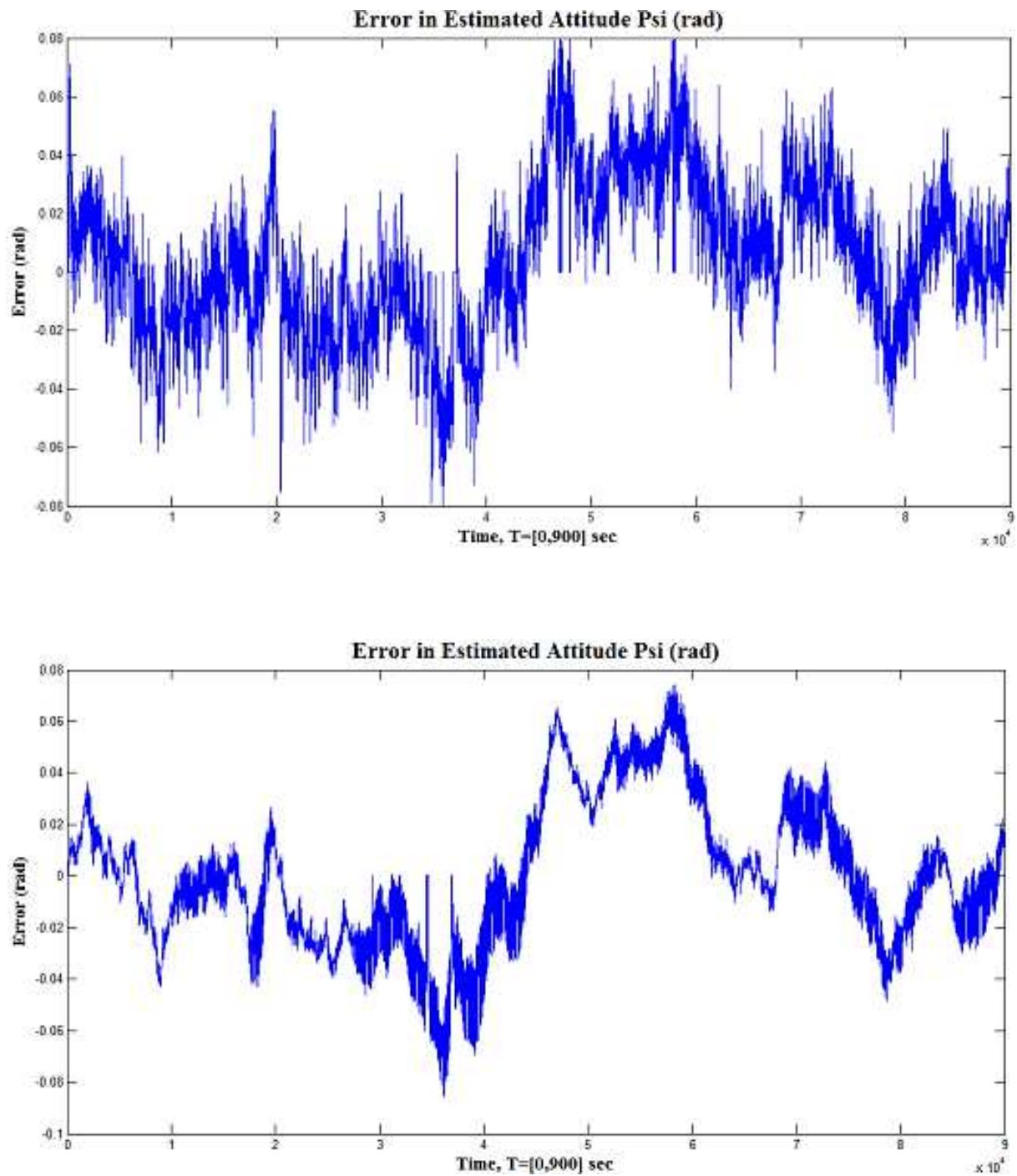


Fig. 18: Comparison of VIG (top) and VIGA (bottom) attitude errors (Psi)

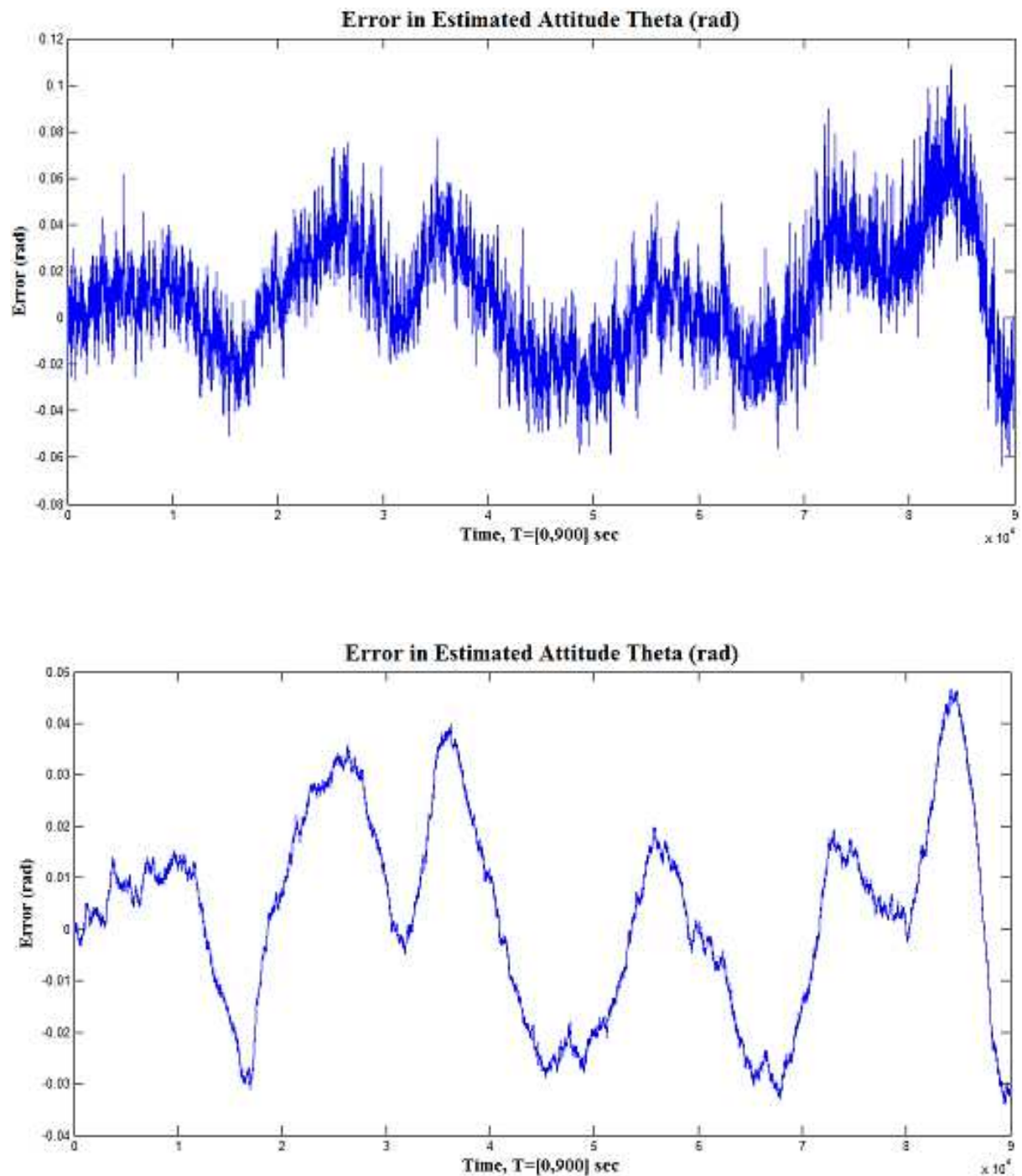
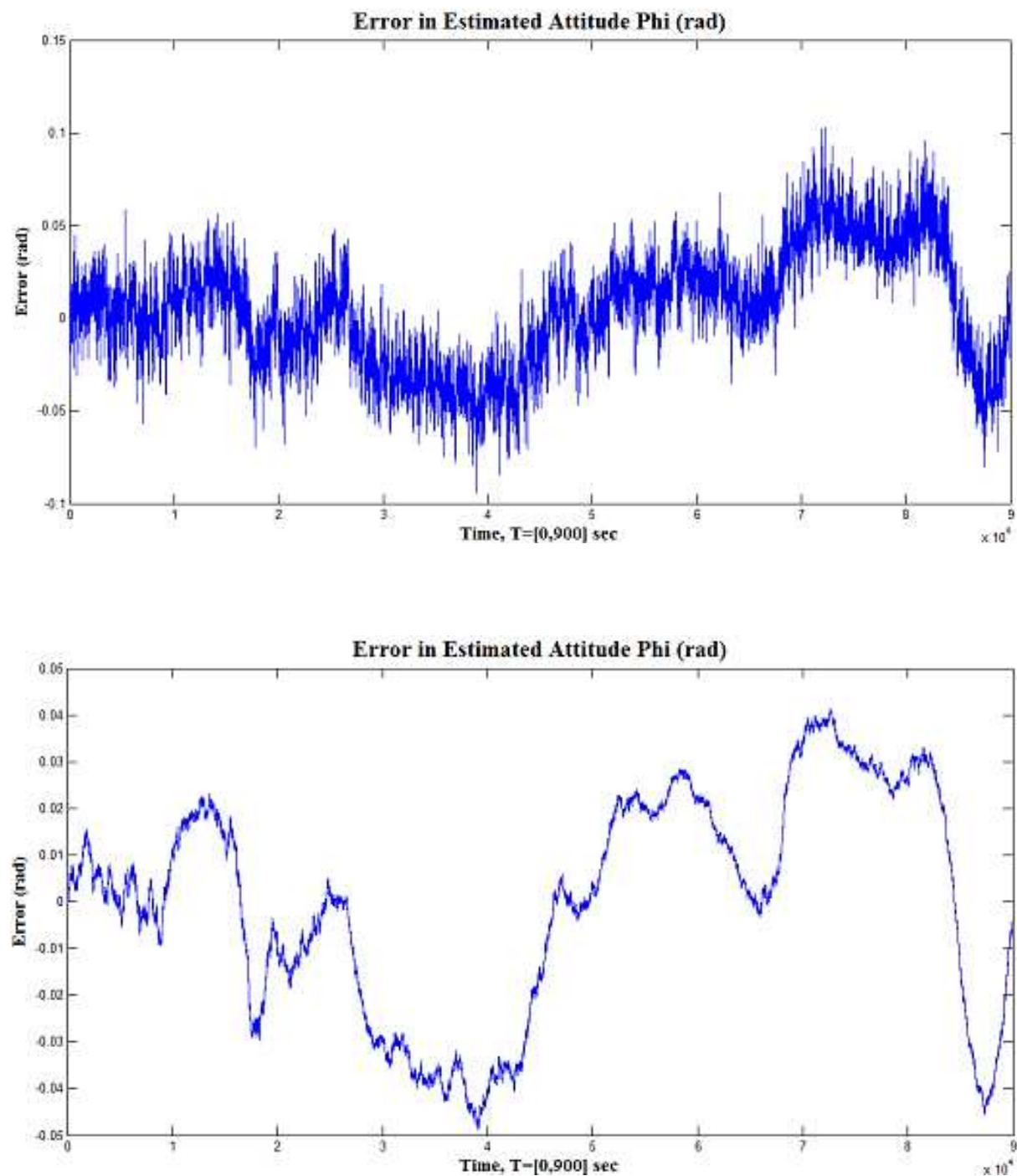
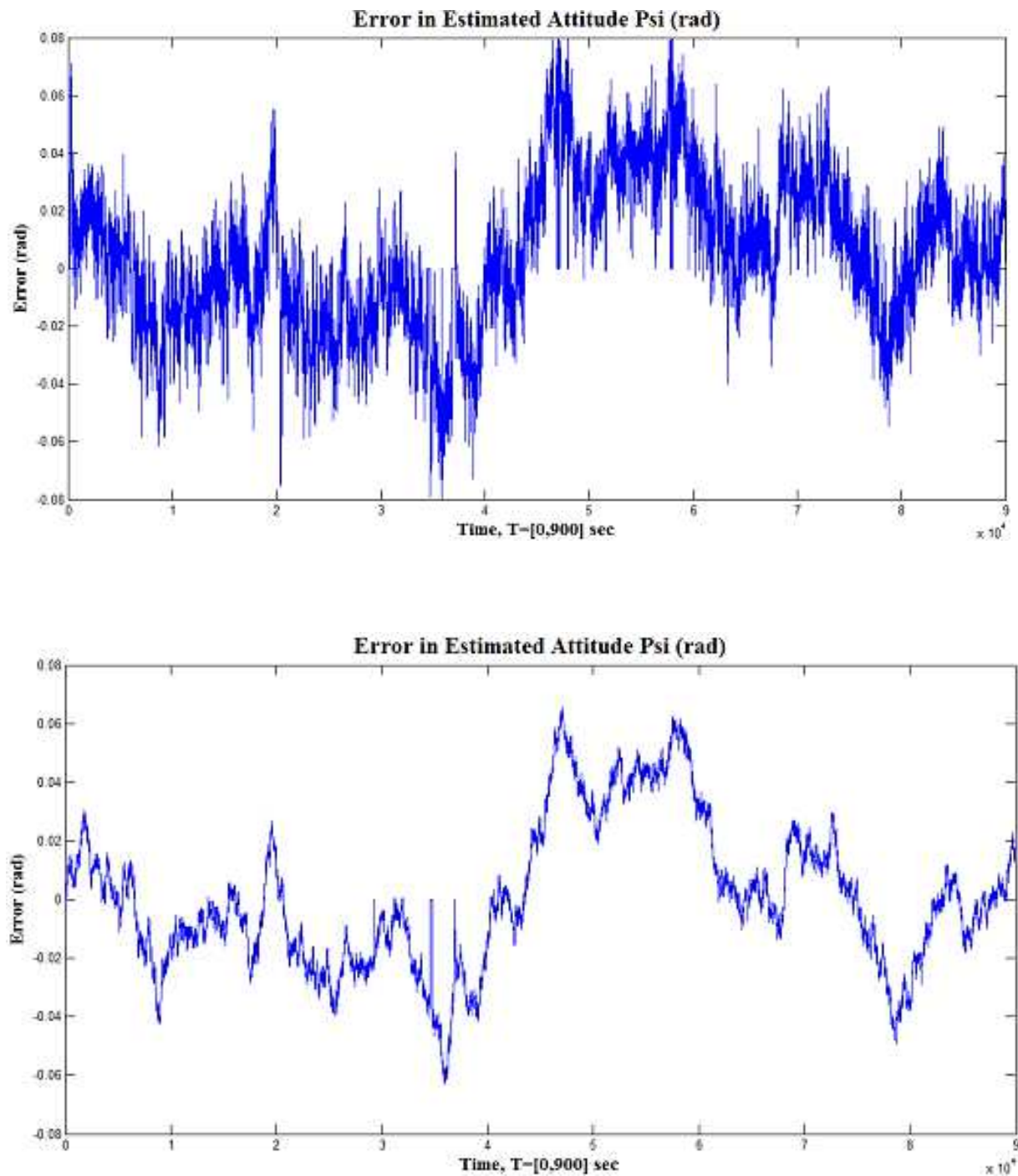


Fig. 19: Comparison of VIG (top) and VIGGA (bottom) attitude errors (Theta)





**Fig. 20: Comparison of VIG (top) and VIGGA (bottom) attitude errors (Phi)**



**Fig. 21: Comparison of VIG (top) and VIGGA (bottom) attitude errors (Psi)**

**Table 7: VIGA attitude error statistics**

Phase of Flight	Pitch ( $\theta$ )		Roll ( $\Phi$ )		Heading ( $\psi$ )	
	Mean (degrees)	$\sigma$ (degrees)	Mean (degrees)	$\sigma$ (degrees)	Mean (degrees)	$\sigma$ (degrees)
Straight Climb (Take-off)	0.0039	0.0038	0.0055	0.0040	0.0112	0.0078
Left Turning Climb	0.0089	0.0028	0.0001	0.0046	-0.0125	0.0142
Straight Climb	0.0014	0.0097	0.0184	0.0031	-0.0066	0.0048
Left Turning Climb	-0.0109	0.0118	-0.0084	0.0153	-0.0040	0.0137
Left Turning Climb	0.0199	0.0065	-0.0089	0.0053	-0.0178	0.0103
Right Turning Climb	0.0231	0.0077	-0.0146	0.0126	-0.0244	0.0073
Level Left Turn	0.0077	0.0100	-0.0349	0.0036	-0.0207	0.0130
Right Turning Climb	0.0238	0.0096	-0.0409	0.0044	-0.0395	0.0147
Straight and Level	-0.0155	0.0093	-0.0175	0.0166	0.0200	0.0251
Right Turning Descent	-0.0132	0.0045	0.0128	0.0070	0.0362	0.0087
Left Turning Descent	0.0083	0.0067	0.0226	0.0032	0.0478	0.0077
Level Right Turn	-0.0167	0.0095	0.0126	0.0107	0.0094	0.0128
Straight Descent	0.0072	0.0088	0.0343	0.0040	0.0082	0.0133
Left Turning Descent	0.0035	0.0013	0.0260	0.0021	-0.0302	0.0082
Right Turning Descent	0.0231	0.0148	0.0208	0.0125	-0.0057	0.0112
Straight Descent	0.0005	0.0247	-0.0305	0.0109	-0.0042	0.0096
All Phases	0.0029	0.0173	-0.0006	0.0240	0.0009	0.0260

**Table 8: VIGGA attitude error statistics**

Phase of Flight	Pitch ( $\theta$ )		Roll ( $\Phi$ )		Heading ( $\psi$ )	
	Mean (degrees)	$\sigma$ (degrees)	Mean (degrees)	$\sigma$ (degrees)	Mean (degrees)	$\sigma$ (degrees)
Straight Climb (Take-off)	0.0039	0.0041	0.0105	0.0041	0.0053	0.0039
Left Turning Climb	0.0096	0.0027	-0.0130	0.0027	0.0005	0.0046
Straight Climb	0.0014	0.0103	-0.0089	0.0103	0.0177	0.0030
Left Turning Climb	-0.0118	0.0133	-0.0032	0.0133	-0.0079	0.0146
Left Turning Climb	0.0210	0.0063	-0.0172	0.0063	-0.0083	0.0046
Right Turning Climb	0.0228	0.0088	-0.0225	0.0088	-0.0158	0.0117
Level Left Turn	0.0061	0.0110	-0.0177	0.0110	-0.0323	0.0037
Right Turning Climb	0.0233	0.0102	-0.0353	0.0102	-0.0394	0.0039
Straight and Level	-0.0181	0.0088	0.0225	0.0088	-0.0135	0.0165
Right Turning Descent	-0.0116	0.0049	0.0352	0.0049	0.0154	0.0059
Left Turning Descent	0.0114	0.0070	0.0458	0.0070	0.0216	0.0038
Level Right Turn	-0.0172	0.0104	0.0080	0.0104	0.0153	0.0103
Straight Descent	0.0112	0.0091	0.0052	0.0091	0.0330	0.0042
Left Turning Descent	0.0064	0.0012	-0.0328	0.0012	0.0255	0.0016
Right Turning Descent	0.0279	0.0149	-0.0073	0.0149	0.0175	0.0144
Straight Descent	-0.0039	0.0276	-0.0011	0.0276	-0.0306	0.0134
All Phases	0.0032	0.0187	0.0009	0.0187	0.0005	0.0232

During the initial VIGA simulation runs, it was evidenced that the ADM data cannot be used effectively without being reinitialised regularly. For the AEROSONDE UAV manoeuvres listed in Table 5, it was found that the optimal period between ADM re-initialisation was in the order of 20 s. Converting VIG and VIGA error statistics to the corresponding RMS (95%) values, it is evident that the ADM virtual sensor contributes to a moderate reduction of the overall attitude error budget in all relevant flight phases. To conclude the simulation data analysis, Table 9 shows a comparison of the VIG/VIGA horizontal and vertical accuracy (RMS-95%) with the required accuracy levels for precision approach as recommended by the International Civil Aviation Organization (ICAO).<sup>[28,29]</sup> The VIG/VIGA accuracy performances are in line with Category Two (CAT II) precision approach requirements.

**Table 9: VIG, VIGA and VIGGA position error statistics**

Category of approach	Horizontal Accuracy (m) 2D RMS-95%				Vertical Accuracy (m) RMS-95% Down			
	Required	VIG	VIGA	VIGGA	Required	VIG	VIGA	VIGGA
CAT I	16	5.2	5.1	5.2	4	2.0	1.9	2.0
CAT II	6.9				2			
CAT III	4.1				2			

## 6. CONCLUSIONS

The research activities performed to design a low-cost and low-weight/volume integrated NGS suitable for small size UAV applications are described. Various candidates were considered for integration with the VBN sensor. GNSS and MEMS-IMUs, with and without augmentation from ADM, were finally integrated into the NGS. The possibility of using GAD system outputs in the data fusion algorithm in small size UAVs is also investigated. Multiple attitude measurements obtained from different antenna locations are used for analysis. The multisensory integration using an EKF is discussed. The attitude/attitude-rate accuracies obtained with the VBN sensor are evaluated by a combination of laboratory, ground and flight test activities. The results are satisfactory in low-level flight and during the approach and landing phases of the UAV flight. AEROSONDE UAV platform is used as a test bed for the test cases. Simulation of the VIG integrated navigation mode showed that this integration scheme can achieve horizontal/vertical position accuracies in line with CAT-II precision approach requirements, with a significant improvement compared to stand-alone SPS GPS. Additionally, simulation of the VIGA navigation mode showed promising results since, in most cases, the attitude accuracy is higher using the ADM/VBS/IMU, rather than using VBS/IMU only. However, due to rapid divergence of the ADM virtual sensor, there is a need for a frequent re-initialisation of the ADM data module, which is strongly dependent on the UAV flight dynamics and the specific manoeuvres/flight-phase transitions performed. In the considered portion of the UAV operational flight envelope, the required re-initialisation interval was approximately 20 s. Results show that there is a moderate accuracy improvement with the use of ADM in a high dynamics environment. Compared to the VIG system, the VIGGA shows an improvement of accuracy in all three attitude angles. The magnitude of this improvement varies for each angle and for different flight phases. As expected, as the number of antennae increases the accuracy improves. The design of the Fuzzy/PID controller was successfully accomplished. However, during the test activities, it was observed that the Fuzzy/PID controller becomes unstable at wind speeds greater than 20 m/s. In case of pure visual servoing during the approach and landing phase, this would lead to the impossibility of tracking the desired features from the surrounding. Current research activities are investigating the modelling of multipath and shielding problems and adequate algorithms are being developed in order to cope with these effects during high dynamics manoeuvres. Furthermore, integrity monitoring functionalities for UAVs are being researched upon to improve the overall system performance. As a result, it is anticipated that the multisensory integrated NGS will be significantly enhanced in terms of data

accuracy, continuity and integrity to fulfil present and likely future RNP requirements for a variety of small UAV applications.

## 7. REFERENCES

1. **ICAO.** (2008). *Performance-based navigation (PBN) manual*. Doc. 9613. Montréal, Quebec. Canada. [crossref](#)
2. **Olivares-Mendez MA, Mondragon IF, Campoy P and Martinez C.** (2010). Fuzzy controller for UAV-landing task using 3D position visual estimation. *Proceedings of IEEE International Conference on Fuzzy Systems*. 18<sup>th</sup> – 23<sup>rd</sup> July. Barcelona. Spain. Pp. 1-8. [crossref](#)
3. **Roumeliotis SI, Johnson AE and Montgomery JF.** (2002). Augmenting inertial navigation with image-based estimation. *Proceedings of International Conference of Robotics & Automation*. Vol. 4. 11<sup>th</sup> – 15<sup>th</sup> May. Washington DC. USA. Pp. 4326-4333. [crossref](#)
4. **Sabatini R, Rodríguez L, Kaharkar A, Bartel C and Shaid T.** (2012). Low-cost vision sensors and integrated systems for unmanned aerial vehicle navigation and guidance. *ARPJ Journal of Systems and Software*. 2(11): 323-349. [crossref](#)
5. **Sabatini R, Rodríguez L, Kaharkar A, Bartel C and Shaid T.** (2012). Carrier-phase GNSS attitude determination and control system for unmanned aerial vehicle applications. *ARPJ Journal of Systems and Software*. 2(11): 297-322. [crossref](#)
6. **Sabatini R, Bartel C, Kaharkar A and Shaid T.** (2012). Design and integration of vision based sensors for unmanned aerial vehicles navigation and guidance. *Proceedings of the SPIE, Optical Sensing and Detection II*. Vol. 8439. 16<sup>th</sup> – 19<sup>th</sup> April. Brussels. Belgium. [crossref](#)
7. **Sabatini R, Rodríguez L, Kaharkar A, Bartel C, Shaid T, Zammit-Mangion D and Jia H.** (2012). Low-cost navigation and guidance systems for unmanned aerial vehicles – Part 1: Vision-based and integrated sensors. *Annual of Navigation Journal*. 19: 71-98. [crossref](#)
8. **Cohen CE, Parkinson BW and McNally BD.** (1994). Flight tests of attitude determination using GPS compared against an inertial navigation unit. *Navigation (ION Journal)*. 41(1): 83-98. [crossref](#)
9. **van Grass F and Braasch M.** (1991). GPS interferometric attitude and heading determination: Initial flight test results. *Navigation (ION Journal)*. 38(4): 297-316. [crossref](#)
10. **Giorgi G, Teunissen PJG and Gourlay TP.** (2012). Instantaneous Global Navigation Satellite System (GNSS)-based attitude determination for maritime applications. *IEEE Journal of Oceanic Engineering*. 37(3): 348-362. [crossref](#)
11. **Pinchin J.** (2011). *GNSS based attitude for small unmanned aerial vehicles*. PhD Thesis. University of Canterbury. Christchurch. New Zealand. [crossref](#)
12. **Cohen CE.** (1992). *Attitude determination using GPS*. PhD Thesis. Stanford University. Stanford. California. [crossref](#)
13. **Keong J.** (2007). *Determining heading and pitch using a single difference GPS/GLONASS approach*. PhD Thesis. University of Calgary. Calgary. Alberta. Canada. [crossref](#)
14. **Xinhua L and Cao Y.** (2003). Research on the application of the vision-based autonomous navigation to the landing of the UAV. *Proceedings of 5<sup>th</sup> International*



- Symposium on Instrumentation and Control Technology*. Vol. 5253. 24<sup>th</sup> – 27<sup>th</sup> October. Beijing. China. Pp. 385-388. [crossref](#)
15. **Todorovic S** and **Nechyba M**. (2005). Dynamic trees for un-supervised segmentation and matching of image regions. *IEEE Transactions on Pattern Analysis and Machine Intelligence*. Pp. 1762-1777. [crossref](#)
  16. **Cornall T** and **Egan G**. (2005). Calculating attitude from horizon vision. *11<sup>th</sup> Australian International Aerospace Congress*. 13<sup>th</sup> – 17<sup>th</sup> March. Melbourne. Australia. [crossref](#)
  17. **Kim J** and **Sukkarieh S**. (2005). 6 DoF SLAM aided GNSS/INS navigation in GNSS denied and unknown environment. *Journal of Global Positioning Systems*. 4(1-2): Pp.120-128. [crossref](#)
  18. **Kais M**, **Dauvillier S**, **Fortellea A**, **Masakid I** and **Laugier C**. (2004). Towards outdoor localization using GIS, vision system and stochastic error propagation. *International Conference on Autonomous Robots and Agents*. 13<sup>th</sup> -15<sup>th</sup> December. Palmerston North. New Zealand. [crossref](#)
  19. **Desouza GN** and **Kak AC**. (2002). Vision for mobile robot navigation: a survey. *IEEE Transactions on Pattern Analysis and Machine Intelligence*. 24(2): 237 – 267. [crossref](#)
  20. **Huang YW**, **Li CY**, **Wu HW**, **Chang HW**, **Hu HW** and **Chian KW**. (2007). Improving the attitude accuracy of a low cost MEMS/GPS integrated system using GPS heading sensors. *Proceedings of the 5<sup>th</sup> International Symposium on Mobile Mapping Technology, ISPRS*. Vol. XXXVI-5/C55. 29<sup>th</sup> – 31<sup>st</sup> May. Padua. Italy. [crossref](#)
  21. **Petovello M**. (2003). *Real-time integration of a tactical-grade IMU and GPS for high-accuracy positioning and navigation*. PhD Thesis. University of Calgary. Alberta. Canada. [crossref](#)
  22. **Godha S**. (2006). *Performance evaluation of low cost MEMS-based IMU integrated with GPS for land vehicle navigation application*. UCGE Report No. 20239. University of Calgary. Department of Geomatics Engineering. Alberta. Canada. [crossref](#)
  23. **Shin EH**. (2005). *Estimation technics for low-cost inertial navigation*. PhD Thesis. University of Calgary. Alberta. Canada. [crossref](#)
  24. **Angrisano A**. (2010). *GNSS/INS integration methods*. PhD Thesis. Parthenope University of Naples. Naples. Italy. [crossref](#)
  25. **Maurer J**. (2012). *Polar remote sensing using an unpiloted aerial vehicle (UAV)*. Seminar by Dr. James Maslanik. Colorado Center for Astrodynamics Research (CCAR). University of Colorado at Boulder. USA. Available online at: <http://www2.hawaii.edu/~jmaurer/uav/#specifications>. (Website accessed in 2012). [crossref](#)
  26. **Unmanned Dynamics LLC**. (2012). *AeroSim aeronautical simulation blockset user's guide*. Available online at: [http://people.rit.edu/pnveme/EMEM682n/Matlab\\_682/aerosim\\_ug.pdf](http://people.rit.edu/pnveme/EMEM682n/Matlab_682/aerosim_ug.pdf). (Website accessed in 2012). [crossref](#)
  27. **Sabatini R**. (1998). *Impiego del GPS per la determinazione d'assetto dei veicoli spaziali, scuola di ingegneria aerospaziale*. Interdisciplinary Research on Satellite Navigation System – Aerospace Systems Design. [crossref](#)

28. **CAA Safety Regulation Group** (2004). *GPS integrity and potential impact on aviation safety*. Paper 2003/09. Civil Aviation Authority. Cheltenham. UK. [crossref](#)
29. **ICAO**. (2006). *Aeronautical telecommunications - Volume 1: Radio navigation aids*. (6<sup>th</sup> ed.). Annex 10 to the Convention on International Civil Aviation. International Civil Aviation Organization. Montreal. Quebec. Canada. [crossref](#)

## 8. NOTATION

ADM	Aircraft dynamics model
ABA	Appearance-based approach
CFM	Carrier phase measurements
CAT II	Category two
COTS	Commercial off-the-shelf
D3	Dull, dirty and dangerous
EKF	Extended Kalman Filter
GADS	GAD system
GM	Gauss-Markov
GNSS	Global navigation satellite systems
GPS	Global positioning system
GAD	GNSS attitude determination
IPM	Image processing module
IMU	Inertial measurement units
INS	Inertial Navigation System
ICAO	International Civil Aviation Organization
KBM	Knowledge-based module
MEMS	Micro-electro-mechanical system
MBA	Model-based approach
NGS	Navigation and guidance system
PBN	Performance based navigation
PVA	Position, velocity and attitude
PID	Proportional/integral/derivative
RNP	Required navigation performance
SLAM	Simultaneous localization and mapping
SPS	Standard positioning service
VIG	VDN/IMU/GPS
VIGA	VIG/ADM
VIGGA	VIG/GAD
VBS	Vision based sensors
WN	White noise
$C_b^n$	Transformation matrix from the body frame to the navigation frame
$e_D$	Yaw error
$e_N$	Roll error
$f^n$	Specific force transformation matrix from inertial frame to navigation frame
$F_{rr}, F_{rv}, F_{vr}$	Matrices
$F_{er}$	Matrix
$K_{k+1}$	Kalman gain matrix at epoch k+1
$P_k$	Covariance matrix
$P_k^+$	Updated values obtained after the correction equations
$P_{k+1}^-$	Predicted value computed by the prediction equations
$q_a, q_g$	Spectral densities
$q_{ba}, q_{bg}$	Spectral densities
$Q_k$	Covariance matrix

$q_{Sa}, q_{Sg}$	Spectral densities.
$R_{k+1}$	Measurement noise covariance matrix
$u_{k+1}$	Innovation vector at epoch $k+1$
$v_E, v_N$	Velocity in east direction, in north direction
$\dot{x}(t)$	Time derivative of the value considered
$x'$	Transformed state error vector
$F(t)$	Dynamic matrix of the system at time $t$
$F', G'$	New dynamics and shaping matrices
$G(t)$	Shaping matrix at time $t$
$h$	Altitude
$H(t)$	Design matrix at time $t$
$k$	Epoch, $k^{th}$ epoch
$R$	Radius of Earth
$t$	Time
$T$	Transition matrix to pass from previous state error vector to new one
$v(t)$	Measurement noise at time $t$
$w(t)$	Process noise at time $t$
$x$	State error vector
$x(t)$	State vector at time $t$
$z(t)$	Measurement (or observation) vector at time $t$
$\delta b_a, \delta b_g$	Accelerometer bias, Gyroscope bias
$\delta P^n$	Position error state
$\delta r^n, \delta P^n$	Position error expressed in terms of latitude and longitude
$\delta S_{ai}$	Scale factor for accelerometers
$\delta S_{gi}$	Scale factor for gyroscopes
$\delta v^n$	Velocity error
$\epsilon^n$	Attitude error term
$\eta_a$	Accelerometer noise
$\eta_{ba}, \eta_{bg}$	Gaussian-Markov process driving noise
$\eta_g$	Gyroscope noise
$\eta_{Sa}, \eta_{bg}$	Gaussian-Markov process driving noise
$\sigma$	Standard deviation
$\sigma_{ba}, \sigma_{bg}$	Gauss-Markov process temporal standard deviations
$\tau_{ba}$	Correlation time for accelerometers
$\tau_{bg}$	Correlation time for gyroscopes
$\tau_{Sa}$	Correlation times for accelerometers scale factors
$\tau_{Sg}$	Correlation times for gyroscopes scale factors
$\phi$	Latitude
$\Phi_k$	State transition matrix from epoch $k$ to $k+1$
$\omega_e$	Angular rate error
$\omega_i^n$	Angular rate transformation matrix from inertial frame to navigation frame